"COMPUTATIONAL STUDIES OF PHYSICAL PROPERTIES OF Nb-Si BASED ALLOYS"

FINAL SCIENTIFIC/TECHNICAL REPORT

Reporting Period July 1, 2010 through December 31, 2013

Lizhi Ouyang

April 16, 2015

DOE Award Number: DE-FE0003798

Principle Investigator: Lizhi Ouyang
Tennessee State University
3500 John A. Merritt Blvd.
Nashville, Tennessee 37209

DISCLAMER

This report was prepared as an account of work sponsored by an agency of the United States Government. Neither the Unite States Government nor any agency thereof, no any of the employees, makes any warranty, express or implied, or assumes any legal liability or responsibility for accuracy, completeness, or usefulness of any information, apparatus, product, or process disclosed, or represents that its use would not infringe privately owned rights. Reference herein to any specific commercial product, process, or service by trade name, trademark, manufacturer, or otherwise does not necessarily constitute or imply its endorsement, recommendation, or favoring by the United States Government or any agency thereof. The views or opinions or authors expressed herein do not necessarily state or reflect those of the United States Government or any agency thereof.

ABSTRACT

The overall goal is to provide physical properties data supplementing experiments for thermodynamic modeling and other simulations such as phase filed simulation for microstructure and continuum simulations for mechanical properties. These predictive computational modeling and simulations may yield insights that can be used to guide materials design, processing, and manufacture. Ultimately, they may lead to usable Nb-Si based alloy which could play an important role in current plight towards greener energy. The main objectives of the proposed projects are: (1) developing a first principles method based supercell approach for calculating thermodynamic and mechanic properties of ordered crystals and disordered lattices including solid solution; (2) application of the supercell approach to Nb-Si base alloy to compute physical properties data that can be used for thermodynamic modeling and other simulations to guide the optimal design of Nb-Si based alloy.

Table of Contents

I. EXECUTIVE SUMMARY 5

II. INTRODUCTION 6

Background 6

III. Methods and Software Developments 8

Prior Work 8

UnitCell Expansion Method for Multicomponent Multi-sublattice Solid Solution System 9

G(p,T) module for calculating temperature dependent properties 12

G(p,T) module for novel uni-axial tensile simulation. 14

IV. Results and Discussions 16

UnitCell Expansion Method 16

Temperature and Pressure Dependent Elastic Constants Calculations 28

Uni-axial tensile simulation 37

Physical properties of Nb-Si based Alloys 38

V. FACILITIES AND RESOURCES 57

I. EXECUTIVE SUMMARY

This report summarizes our method development, software implementation, infrastructure improvement and computational studies for the Nb-Si based alloys system during the three and half year period over which we have developed coarse-grained cluster expansion approaches for modeling disorders and applied them to investigate structure-properties relation alloys.

We have developed three methods which are implemented as modules in our G(p,T) package:

- **Supercell method**. The large supercell models provide configuration freedom for calculating the carbon distribution.
- **Unitcell expansion method**. Rigorous approach such as cluster expansion method is computationally prohibitive for boron carbide as partial occupations can be found on all 15 lattice sites. To overcome the challenge of complex lattices, we developed a coarse-grained unitcell expansion method in which each unitcell is considered a site thus greatly reduces the lattice complexity at the expense of more types at each site.
- **Uniaxial tensile simulation.** Uniaxial tensile simulation under novel constraining conditions which permits slipping was developed.

Additional modules for physical properties calculations are also developed:

- **Pressure dependent elastic constants**.
- **Structure modeler that generate supercells, surface slabs and interfaces**.
- Input generator for first principles calculations based on our internal structure format.
- Job manager for automating and parallelizing the complex physical properties calculations that involves many different kinds of input setups for those first principles calculations.

To facilitate our software development, we had built an 18-node computer cluster (gpt.tsuniv.edu) with off-the-shell components with total budget less than $10K.

II. INTRODUCTION

Background

Nb-Si based alloys are highly promising candidates for next generation hot section material enabling turbine engine operating at temperature above 1350°C[1]. Monolithic Nb has an array of attractive properties for high temperature applications including a very high melting point 2469°C, a relatively low density 8.56g/cm^3, a low ductile-brittle-transition-temperature(DBTT)<-100°C, and good ductility at room temperature. But it suffers from low oxidation resistance at high temperature[2] and modest high temperature mechanical properties[3]. Alloying with Si introduces intermetallic phases Nb_3Si and/or Nb_5Si_3 which significantly improve high temperature mechanical properties and lower the density further to a range from 6.6 to 7.2g/cm^3. The intermetallic phases have a high melting point >1750°C but are brittle at room temperature. By incorporating a ductile Nb solid solution phase, the resulting *in situ* Nb/Nb Silicide composite can be strengthened through the ductile phase toughening mechanism. However, high creeping rate, low oxidation resistance, and insufficient fracture toughness remain the biggest roadblocks towards their eventually industry acceptance. Alloying with a third element such as Al, Cr, or Ta leads to a Cr_2Nb type Laves phase which has shown to improve oxidation resistance[4]. More alloy elements have been studied to further improve the Nb-Si base alloys to satisfy the requirements of the targeted high temperature applications [1, 4-7]. Up to date, the evolution of Nb-Si alloy developments has now reaches a stunning complexity with often more than seven elements in those alloys[8]. Still, a Nb-Si based alloy with a well balanced set of properties that are suitable for commercial applications remains to be found.

One key requirement for optimal alloy design is to have a detailed knowledge of physical properties including thermodynamic, kinetic, structural and mechanical properties of all phases involved and their corresponding phase field. Traditionally, these data are mainly obtained through careful experimental measurements. As more elements are adding to improve the Nb-Si base alloy, the complexity of the

phases involved increases dramatically. It has been shown that adding Mo into the Nb-Si alloy can affect stability order of Nb silicide phases [9]. Interfaces may also be modified by additional alloy elements. Geng et al observed that addition of Al to the Nb-Si-Cr system causes the Laves phase to precipitate at the interface between Nb solid solution and Nb silicide[6]. In addition, microstructure of the Nb-Si based alloy can be significantly altered by the added alloy elements [1, 10]. The cost and time required to conduct these required experiments can increase prohibitively. Hence there is a strong demand for accurate computational studies to supply part of the required knowledge which can potentially lower the cost and speed up the developing cycle significantly.

In the past few decades, thermodynamic modeling using the CALculation of PHAses Diagram (CALPHAD) method[11] which uses all thermodynamic data obtained from various means to predict phases diagram has evolved into a basic tool for material development. The success of CALPHAD method relies on accurate phase equilibria and thermochemistry data particularly the Gibbs free energy of the phases involved. For the Nb-Si base alloys, the lack of reliable thermochemistry data for the more complex ternary and quaternary alloys have been a major challenge for optimal alloy design.

Owing to their predictive power, first principles based approaches have often been employed to compute physical properties of the alloy phases including mechanical, thermodynamic, and electronic properties. The two basic challenges of using first principles methods for these physical properties calculations are: (1) structural modeling; (2) temperature dependent thermodynamic properties calculation. Often the structural models of the phases involved are very complex or even unknown. For example, we may find grain boundaries, amorphous phases, phases with various defects and solid solution phases, *etc* in the alloys. These complex phases require very large atomistic models to properly describe their structures.

In this project, we addressed two important issues in structure modeling and temperature dependent thermodynamic properties calculations: (1) modeling of solid solution system; (2) temperature pressure dependent elastic properties calculations.

III. Methods and Software Developments

Prior Work

Lattice dynamics with the G (P, T) package

We had developed the G(p,T) package capable of computing elastic tensor, phonon structure, Helmoltz and Gibbs free energy and many other thermodynamic properties such as entropy, heat capacity, isothermal bulk modulus, thermal expansion coefficient, and Grüneisen parameters, etc. The G(p,T) package were parallelized at task level and successfully tested on supercomputers of NERSC.

G(p,T) package was implemented as an easy-deploy script based job management and automation system. It included an elastic properties module, a phonon calculation module, a Born effective charge module, an optical and dielectric properties module, a job management and automation module, and a box of analysis and graphic tools for phonon, thermodynamic properties, elastic waves, and dielectric properties *etc*. G(p,T) calculates the free energy of solid with Born-Oppenheimer approximation that separates electron and ion motion. Electronic contribution to free energy is calculated using first principles method such as VASP [12-14]. Ionic contribution to free energy is calculated using semi-classical lattice dynamic approach. Volume dependent lattice free energies were calculated using quasi-harmonic approximation in which the lattices were considered harmonic at each volume and free energies of harmonic lattices can be calculated from their force constant matrices. G(p,T) package computes the force constant matrix using finite difference approach with energy and force evaluated by a first principles method. Phonon structure is then obtained from the dynamic matrix constructed based on force constant matrix. Once phonon spectrum is obtained, it is possible to estimate all other thermodynamic functions. The free energy *F(V,T)* at temperature *T* and volume *V* is given by,

$$
\begin{aligned}
&F(V,T) = F^{elec}(V,T) + F^{vib}(V,T) = U^{elec}(V,0) + F^{elec,T}(V,T) + F^{vib}(V,T) \\
&F^{elec,T}(V,T) \approx -\sum_i k_B T \ln(1 + e^{(\varepsilon_F - \varepsilon_i)/k_B T}) + \sum_{\varepsilon_F \geq \varepsilon_i} (\varepsilon_F - \varepsilon_i) \\
&F^{vib}(V,T) \approx \sum_q^{BZ} \sum_i^{3N} \{\tfrac{1}{2}\hbar\omega_i(V,q) + k_B T \ln(1 - e^{-\hbar\omega_i(V,q)/k_B T})\}
\end{aligned}
\qquad (1)
$$

where $F^{elec}(V,T)$, $F^{vib}(V,T)$, $U^{elec}(V,0)$, and $F^{elec,T}(V,T)$ are electronic free energy, vibrational free energy, internal energy, electronic excitation free energy, ε_F is the Fermi energy, ε_i is the *i*th energy of fermions, $\omega_i(V,q)$ is the round frequency of *i*th branch of bosons at wave vector *q*.

Other thermodynamic properties can also be calculated from the above obtained Helmholtz free energy, for example, entropy $S = -(\partial F/\partial T)_V$, pressure $P = -(\partial F/\partial V)_T$, Gibbs free energy $G=F+PV$, constant volume specific heat $C_V = T(\partial S/\partial T)_V$, volume thermal expansion coefficient $\alpha_V(T) = d\{\ln V(T)\}/dT$, isothermal bulk modulus $B(T) = -1/(d[\ln V(T)]/dP)$, thermal Grüneisen parameter $\gamma_{th} = V\alpha_V(T)\,B(T)/C_V$, and constant pressure specific heat $C_P=(1+ \gamma_{th}\,\alpha_V(T))C_V$.

The G(p,T) package has been successfully used in elastic constants studies of common ceramics[15], the prediction of a novel phase of SiO_2 in which a similar supercell approach was applied on modeling solid solution zirconium silicate $(ZrO_2)_x(SiO_2)_{1-x}$[16, 17]. More recently similar work has recently been performed on mullite-type lattice of alumina[18].

Software Modules Implemented During the Project Period

We implemented additional automation modules within our G(p,T) package to meet the challenge of carrying out large number of complex first principles calculations required for sufficient sampling of the configuration space using large supercell models for disordered crystals.

UnitCell Expansion Method for Multicomponent Multi-sublattice Solid Solution System

In traditional cluster expansion method, the energy was expressed in terms of atomic clusters. In practices, a maximum complete cluster set γ is used as cut off in the energy expression,

$$E(\vec{\sigma}) \cong \sum_{\alpha \in \gamma} V_\alpha \Phi_\alpha(\vec{\sigma}) \qquad (2)$$

where $\vec{\sigma} = \langle \sigma_1, \sigma_2, \cdots, \sigma_N \rangle$ is the configuration vector, α is a cluster in γ, σ_i is the site occupation variable at *i*th lattice site, V_α is the effective cluster interaction coefficient, and $\Phi_\alpha(\vec{\sigma})$ is the cluster

function of cluster α. The above approach has been extensive used to study binary alloys. However, if the lattice is complex and many non-equivalent lattice sites existed in the structure, the traditional cluster expansion method can be computationally expensive if not prohibitive. In the case of boron carbide, where carbon atoms could reside randomly on the stable conjugated icosahedra, the maximum cluster can be exceedingly large as huge maximum cluster set with clusters up to 12 atoms may be needed.

We propose to express the energy of the disordered crystal in terms of primitive unitcell,

$$E(\vec{\eta}) \cong \sum_{\beta \in \varsigma} V_\beta \Phi_\beta(\vec{\eta}) \tag{3}$$

where ζ is the maximum complete cluster set of unitcells, β is a cluster in ζ, $\vec{\eta} = \langle \tau_1, \tau_2, \cdots, \tau_L \rangle$ is the configuration vector, $\tau_i = \tau\left(\sigma_1^{(i)}, \sigma_2^{(i)}, \cdots, \sigma_{n_i}^{(i)}\right)$ is *i*th unitcell configuration variable, V_β is the effective unitcell cluster interaction coefficient, and $\Phi_\beta(\vec{\sigma})$ is the unitcell cluster function of cluster β. Energy expansion in terms of unitcells trades the complexity in lattice for increased component types. For one unique site simple lattice such as BCC/FCC, UEM reduces to traditional cluster expansion method. For complexity lattice, particularly large unitcells, UEM has significant advantages. First, it is possible to reduce the number of unique unitcell types, n_τ . For a given concentration, we can carry out an extensive in unitcell or small supercell calculations to identify the lowest configurations that will be used in the UEM calculations. Second, if the unitcell is large enough, it is possible only small clusters up to near-neighbor clusters or at most triplets will be needed in the energy expression, thus the total number of effective cluster interaction coefficients (ECI) N_{β, n_τ} , remains manageable (~$n_\tau^{2\sim3}$). Third, it is quite simple to introduce lattice defects, surface structures in this approach.

If only considering the nearest neighbor interaction, the UEM becomes a Potts model. Potts models is a generalized Ising model in which a finite set of symbols, here we referred as unique unitcell types, is used to defined to the lattice site occupations,

$$H_g = -\sum_{(i,j)} J_{ij} \delta(\tau_i, \tau_j) - \sum_i h_i \tau_i \tag{4}$$

where J_{ij} is the near-neighbour interaction, h_i is the self-interaction energy coefficient of *i*th lattice site.

If only considering the nearest neighbor interaction, the UEM becomes a Potts model. Potts models is a generalized Ising model in which a finite set of symbols, here we referred as unique unitcell types, is used to defined to the lattice site occupations,

Unitcell expansion method (UEM) implementation: Discrete Chebyshev polynomials.

The cluster interactions are not independent. Direct fitting of supercell energies to clusters tends to have numeric instability problems. Moreover, the convergence of such direct energy expansion is poor. To accelerate the convergence of the energy expansion, we transform these interactions into new effective cluster interactions (ECIs) on a complete orthonormal basis. Our current implementation uses the discrete Chebyshev polynomials .

Considering a cluster with N lattice points, each point p is characterized by an occupation number $\sigma_p = \pm 1, \pm\frac{m-1}{m}, \ldots, \pm\frac{1}{m}, (0)$ for a system with M different components, where M = 2m (or 2m+1). A configuration of the cluster in real space can then be expressed as a vector of occupation numbers $\sigma = \{\sigma_1, \sigma_2, \ldots, \sigma_N\}$ and energy is a function of $\boldsymbol{\sigma}$. We used the M discrete Chebyshev polynomials to describe the point variables on orthonormal basis space. For each lattice point p the orthogonal polynomial is defined by

$$\Theta_{2s}(\sigma_p) = \sum_{k=0}^{s} c_k^{(s)} \sigma_p^{2k}, \qquad s = 0, 1, \ldots, m-1, (m), \tag{5}$$

$$\Theta_{2s+1}(\sigma_p) = \sum_{k=0}^{s} d_k^{(s)} \sigma_p^{2+1}, \qquad s = 0, 1, \ldots, m-1, \tag{6}$$

where the coefficients $c_k^{(s)}$ and $d_k^{(s)}$ must agree with the orthogonally relations,

$$\langle \Theta_n(\sigma_p), \Theta_{n'}(\sigma_p) \rangle = \delta_{nn'} \tag{7}$$

where the inner product of any two functions of $\boldsymbol{\sigma}$, $f(\boldsymbol{\sigma})$and $\mathbf{g}(\boldsymbol{\sigma})$is defined as

$$\langle \mathrm{f}(\boldsymbol{\sigma}), \mathrm{g}(\boldsymbol{\sigma}) \rangle = M^{-N} \sum_{\sigma_1} \sum_{\sigma_2} \dots \sum_{\sigma_N} \mathrm{f}(\boldsymbol{\sigma}) \cdot \mathrm{g}(\boldsymbol{\sigma}) \tag{8}$$

The coefficients $\mathbf{c}_{\mathbf{k}}^{(\mathrm{s})}$and $\mathbf{d}_{\mathbf{k}}^{(\mathrm{s})}$ can be obtained using the Grad-Schomidt algorithm for over-determined systems.

Any structure determined property can then be represented as the linear function of the cluster functions in the system,

$$\mathrm{F} = \sum_{\alpha} \sum_{s} \Phi_{\alpha s} \mathrm{K}_{\alpha s} \tag{9}$$

where the $K_{\alpha s}$ are the effective cluster interactions (ECIs). We assume this variable only relative with the local interactive clusters, so the system size has no effect on ECIs. We can calculate the ECIs on small systems which the first principle method can handle with, and then applied to large systems.

UEM implementation in G(p,T) package

The UEM implementation consists of five programs and related scripts. The first step in a UEM calculation is to build the unitcell list. Our approach is to exhaustively calculate formation energy of unitcells at a given concentration. The formation energies are then ranked and the lowest few are selected for the UEM calculation. It is possible to examine the stability of the result by including more unitcells in the UEM calculations.

G(p,T) module for calculating temperature dependent properties.

We implemented a pressure dependent elastic constants calculation module. Ab initio force calculations are the bases for theoretical evaluation of mechanical, elastic and vibrational properties. In the G(p,T) package, the elastic constants C_{ij}(P,T=0) at a given pressure P are calculated from the following equation,

$$C_{ij}(P,T=0)=\left.\frac{\partial^2 U(\{e\})}{\partial e_i \partial e_j}\right|_{\frac{\partial U(\{e\})}{\partial e_i}=-P\boldsymbol{\lambda}_i} \quad \text{where } \lambda_i=\begin{cases}1, i=1,2,3\\ 0, i=4,5,6\end{cases} \tag{10}$$

where U({e}) is the total energy of a given periodic structure represented by a strain {e} relative to a reference structure.

To calculate the elastic constants C_{ij}(P,T=0), U({e}) has to be evaluated in a six dimension strain parameter space, which can be computationally prohibitive if the full parameter space is to be explored. If only elastic constants at hydrostatic pressures are to be calculated, the computational complexity can be greatly reduced since the total energy calculations are limited to the strain space within the proximity of the structures under hydrostatic pressures. We calculate the hydrostatic pressure and elastic constants in the following steps. (1) A zero temperature equation of state is calculated to estimate the periodic cell volume range corresponding to the targeted pressure range. (2) A series of structures covering the volume range estimated from the targeted pressures are first optimized at zero temperature as the reference structures $\{\boldsymbol{e}\}_0^k$ where *k* is the index of the reference structure. (3) A set of strains in the form of $x\sum_{i=1,6} a_i \hat{\boldsymbol{e}}_i$, where *x* is a small factor, a_i is a constant, and $\hat{\boldsymbol{e}}_i$ is the strain basis, are applied to the reference structure. The total energies of the strained structures $\{\boldsymbol{e}\}_j^k$, where *j* is the index of strain, are calculated using the total energy module in the G(p,T) package. Symmetry is explored to reduce the number of strains and to maintain as higher symmetry as possible in the strained structure. (4) The obtained total energies of the strained structures $U(\{e\}_j^k)$ are used to fit against the free energy model,

$$U(\{e\}_j^k)=U(\{e\}_j^k)-V(\{e\}_j^k)\boldsymbol{\sigma}(\{e\}_j^k)\boldsymbol{\varepsilon}+1/2V(\{e\}_j^k)\boldsymbol{\varepsilon}C(\{e\}_j^k)\boldsymbol{\varepsilon}+O(\boldsymbol{\varepsilon}^3) \tag{11}$$

where $V(\{e\}_j^k)$, $\boldsymbol{\sigma}(\{e\}_j^k)$, and $C(\{e\}_j^k)$ are the volume, strain, stress and elastic constants tensors, $O(\boldsymbol{\varepsilon}^3)$ is the higher order error term. From the free energy model, we locate the strained structure $\{\boldsymbol{e}\}_P^k$ with hydrostatic pressure $\boldsymbol{P^k}$ on the energy surface. For a quadratic energy model, we have:

$$V(P^k)C(P^k) = V(\{e\}_P^k)C(\{e\}_P^k) = V(\{e\}_0^k)C(\{e\}_0^k) \qquad (12)$$

assuming $\{\boldsymbol{e}\}_P^k$ is at the close proximity of $\{\boldsymbol{e}\}_0^k$. It is possible to include higher order terms in the total energy model but the computational costs will be significantly larger since much more parameters will be included in the total energy model. Step 4 is repeated for each reference structure to obtain the pressure dependent $C_{ij}(P^k)$. This approach as implemented in the G(p,T) package can be applied to any symmetry type of solids.

G(p,T) module for novel uni-axial tensile simulation.

Calculation of ideal tensile strength of crystal using first principles method is mostly carried out with a small unitcell. Depending on the tensile direction, the unitcell is chosen based on known deformation pathways related to a particular crystal symmetry break[19-21]. The tensile test is simulated by applying strain or stress to the unitcell. In practice, the unitcell is to be relaxed under either fixed strain or fixed stress and a uniform strain is applied to the whole unitcell.

One serious drawback of current approach is that it does not allow non-uniform strain pathway, for example, slipping and rotation of the crystal. Up to now, the methods used to calculate the ideal tensile strength are often either unrealistic or unreliable, for example, most ideal tensile strength calculations show failure at strain of more than 10%. It is well known that metal accommodates strain by dislocation. These small unitcell models prevent slipping since small model means the slipping planes have to be forbiddingly dense.

To circumvent the problem, we use a much larger supercell model which allows the slipping planes to be separated by about 10-20Å. Under uniaxial tensile stress, the supercell model will be able to slip along their preferred direction. A rotation of the supercell model is necessary to maintain the orientation of the model so that a large vector along the uniaxial tensile direction remains in the same direction. Figure 1 illustrates the deformation of a unitcell under uniaxial stress.

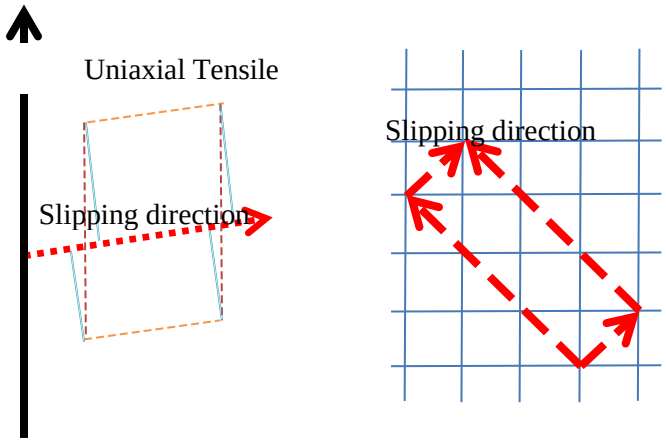

Figure 1 Left: Deformation of the unitcell under uniaxial stress. Right: supercell setup. The larger supercell is to ensure large separation between the slipping planes in the periodic cell.

We developed a module in G(p,T) that are capable of simulating tensile test which allows non-uniform strain pathways to be examined. In our scheme, uni-axial tensile simulation can be carried out in both fixed overall strain and fixed stress conditions. In both cases several small non-uniform symmetric-breaking initial strains are applied to the non-deformed supercell, the supercell is then relaxed under either constant cell parameters or constant stress conditions. The non-uniform initial strain may lead to different deformation pathways and different final energies.

The constant stress relaxation algorithm implemented in VASP applies consecutively small strains on the cell based on the stress calculated at each step,

$$C_{n+1} = (I + \mu(\sigma_n - \sigma_T)C_n \qquad (13)$$

where C_n is the supercell lattice matrix at step n, σ_n is the stress tensor at step n, σ_T is the targeting stress tensor, I is the identity matrix, and μ is a small step factor. Even though the stress tensor is symmetric, the

consecutively multiplication of symmetric matrix leads to non-symmetric transformation to the original cell. Therefore the algorithm leads to rotation which is particularly problematic when the symmetric of the crystal is low.

To prevent unrestricted rotation, we implemented in the G(p,T) module, a new algorithm for constant stress simulation in which the cell parameters are updated according to,

$$C_{n+1} = (I + \mu(\sigma_{n|T} - \sigma_T))C_n \qquad (14)$$

where $\sigma_{n|T}$ is the modified stress tensor at step *n* to ensure a vector along the tensile direction remaining in the same direction thus preventing arbitrary rotation.

IV. Results and Discussions

We use the following accuracy setting for all VASP calculations: (1) planewave energy cutoff is 400eV; (2) energy convergence is 10^{-8}eV/cell and force convergence is 10^{-5}eV/Å; (3) use reciprocal mesh for charge density representation.

UnitCell Expansion Method

Boron Carbide

Boron carbide is a complex multi-sublattice binary solid solution. Figure 2 illustrates the primitive rhombohedra cell of boron carbide which consists of 15 sublattice sites and all of them can be occupied by either Boron or Carbon. There will be about 2^{15}= 32768 possible configurations if carbon is allowed at all sites in the 15-atom rhombohedra primitive unitcells. For feasible unitcell expansion method

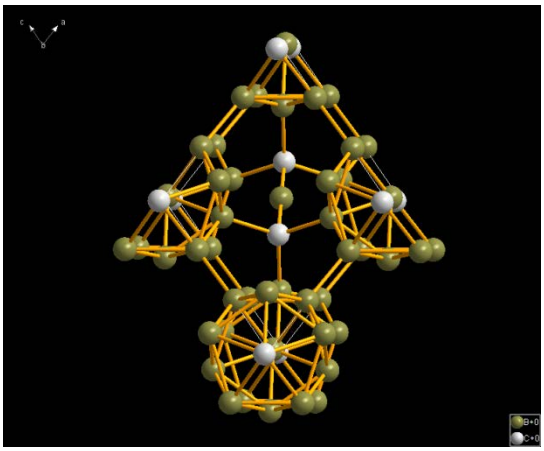

Figure 2. Ball-stick model of a 15 atom crystal model of B_4C. Gray and white represent B and C, respectively.

calculation, it is necessary to reduce the candidate unitcell configurations. Figure 3 plots the energy and pressure of all possible unrelaxed primitive unitcell models with 1 to 5 carbon atoms which correspond to 6.67% to 33.3%. Experimental unitcell parameters are used in these calculations. We selected total 16 primitive cells from all concentrations calculated.

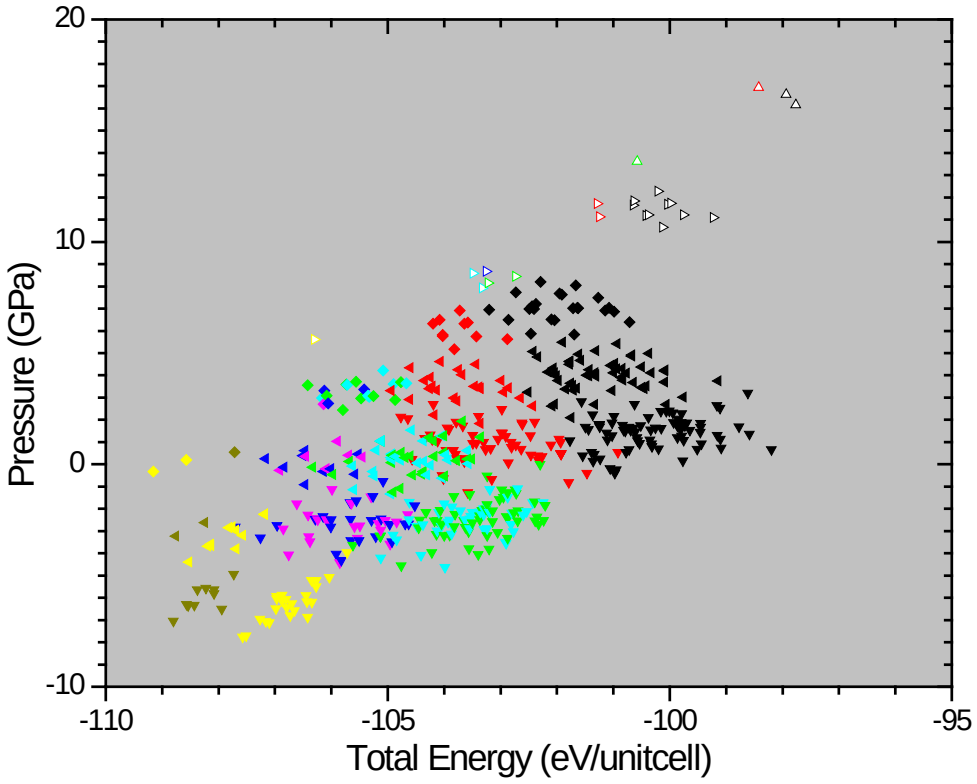

Figure 3. Total energy and pressure plot of all un-relaxed $B_{12-x}C_{3+x}$ primitive cells with x=-2,-1,0,1,2. The color indicates the structure of the 3-atom chain. The shapes of the symbols, up triangle, right triangle, diamond, left triangle, and down triangle, correspond to primitive cell structures with x=-2,-1,0,1,2, respectively. The colors of the symbols, dark yellow, yellow, magenta, cyan, blue, green, red, and black, represents C-C-C, C-B-C, B-C-C, B-B-C, C-C-B, C-B-B, B-C-B, and B-B-B, respectively. Clearly the C-C-C and C-B-C are the energetically favored 3-atom chain configurations for all allowable range of x. When there is only one carbon in the unitcell, it prefers to reside at either end of the 3-atom chain.

In current study, we only consider the cluster with 1 or 2 pseudo-atoms since the primitive cells of boron carbide are quite large. There are 16 kinds of functions of the clusters containing 1 pseudo-atom. Because a pseudo-atom has 6 neighbors with same face, 12 neighbors with same edge, and 8 neighbors with same point, theoretically, there are 26 kinds of clusters containing 2

pseudo-atoms. However, the number of clusters can be reduced by exploiting the symmetry. We cannot tell the difference between two clusters which are symmetrically equivalent, so we can say the cluster functions are same with each other. In boron carbon system, we have 5 different kinds of clusters (2 pseudo-atoms) after considering the symmetry. Thus the number of cluster functions with two pseudo-atoms are 680, and the total number of cluster functions we considered is 696.

In principle any extensive properties of the lattice model can be represented as the linear function of the cluster functions in the system (Equation 9). We calculate the ECIs based on properties of small supercells which are computationally feasible. The obtained ECIs are then applied to large supercell Monte Carlo simulations to estimate their properties.

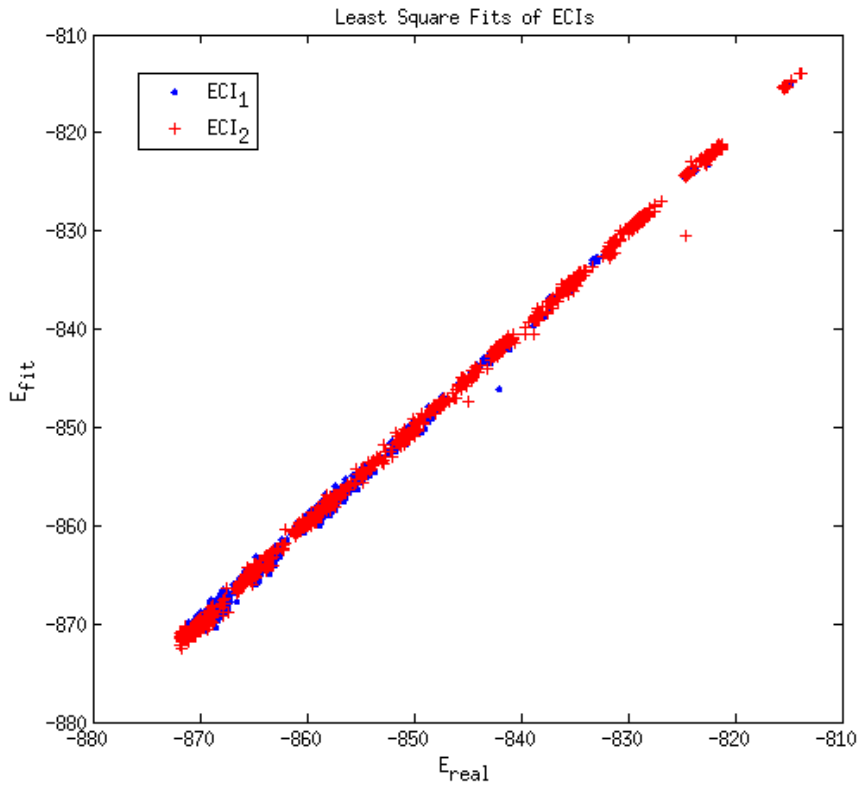

Figure 4 The energies of two groups of small systems calculated from DFT (E_{real}) and cluster expansion method (E_{fit}).

We calculate the energies of small training systems with 8 pseudo-atoms (120 atoms) using VASP with the common accuracy setting. The energy of the small supercell is expressed in terms of cluster functions,

$$\vec{\mathrm{E}} = \boldsymbol{\Phi}\vec{\mathrm{K}} \tag{14}$$

where $\vec{\mathrm{E}}$ is the energy vector whose elements are energies of small supercells. $\boldsymbol{\Phi}$ is a matrix, of which every row represents the cluster functions of every small system. $\vec{\mathrm{K}}$ is the ECIs, which can be estimated by least square linear fit method. Figure 4 shows two groups of energies calculate from DFT and cluster expansion. Each group contains 1000 systems composed of 120 atoms. The energies from DFT is treated as "real" energies (E_{real}) of the systems and those from cluster expansion is showed as a "fitting" energies (E_{fit}). The figure shows that two groups of energies from different calculation method meet very well, which means the energy can be expanded on cluster basis.

A cross-validation method can be used to decide whether the ECIs is effective on calculating the unknown system's properties. We use part of the training data to estimate the ECIs, then use these estimated ECIs to predict the other training data. Figure 5 shows the cross-validation results of two groups of systems (1000 training data of each system). These two groups of energies also meet very well.

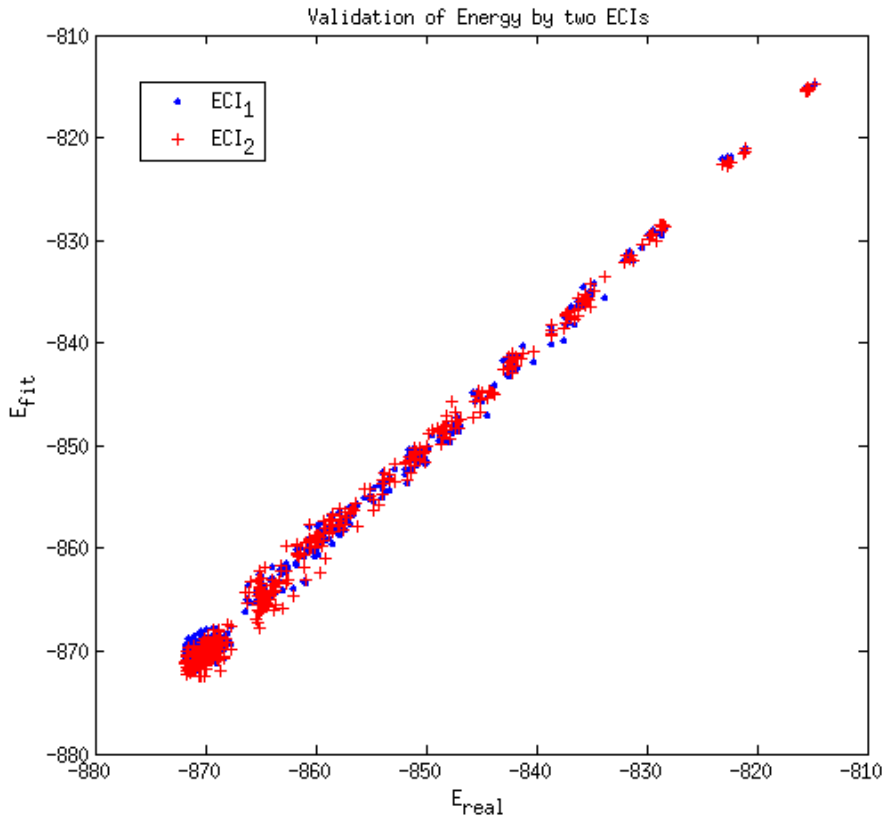

Figure 5 The energies of two groups of small systems from DFT (E_{real}) and cluster expansion method using ECIs (E_{fit}) from each other

Figure 6 shows the relative error of the energies from cluster expansion. First, we can see the relative error is always less than about 2.2%. It is a very precise method to calculate energy. Second, if we use more training data, e.g. twice the number of ECIs, the relative error can be reduced to about 1.6% or even less. That is, if possible, we can use more training data to improve the precision of the results.

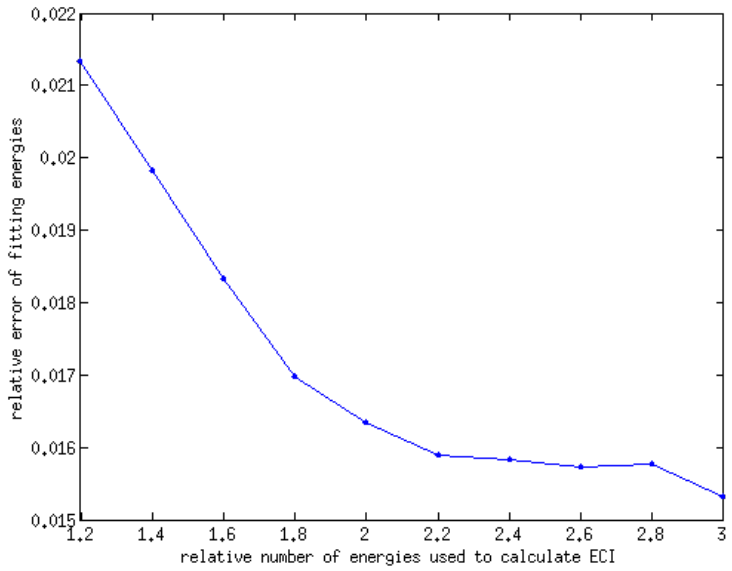

Figure 6 Average relative error of the energies calculate from cluster expansion method vs. the relative number of training data ($n_{training}/n_{ECIs}$)

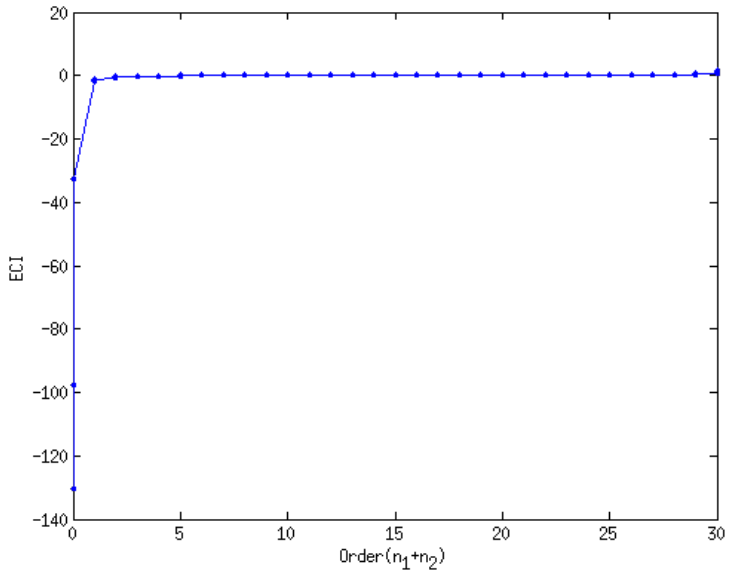

Figure 7 The value of ECIs vs. the order of cluster functions

We can define the cluster function's order: , $\sum(\mathbf{n}, \mathbf{n}', \ldots, \mathbf{n}'')$ which is the sum of the highest exponents of the basis in the lattice functions. Figure 7 is the relationship of the values of ECIs with the cluster functions' orders. Most ECIs with high orders (> 2) have near 0 value, which means they contribute less to the systems energy. If the computation capacity is limited, we can use only the ECIs with low orders and still get acceptable results.

After the ECIs are estimated, we can integrate the cluster expansion method into traditional Monte Carlo simulation to calculate system's properties. Here we study the relationship of free energy and the components of boron carbon material of large size. The system size we used is composed of 125 000 pseudo-atoms (1 875 000 atoms), while the percentage of carbon is from 6.67% (1 carbon atom per pseudo-atom) to 26.67% (4 carbon atoms per pseudo-atom). The system is so large that calculating the energy directly is impractical. Thus we use cluster expansion method to predict energy instead of traditional ways, such as DFT etc.

We start from a system with a random configuration with a certain percentage of C, and calculate the initial energy. In every step we randomly choose two atoms and change them to other possible atoms under the constraint that the number of C does not change. The new energy of the new configuration can also be calculated by cluster expansion method, and then Metropolis algorithm is used to determine whether new configuration is accepted. The evolving process can be repeated for long enough time and after the system achieves equilibrium state the time average configuration energy is a good approximation of the system's free energy.

Figure 8 shows the energy evolution of the system with 6.67% C under different temperature (300K, 1000K , and 2000K). It is easy to see that under low temperature, the system has low energy, but high temperature make the system easy to be equilibrium.

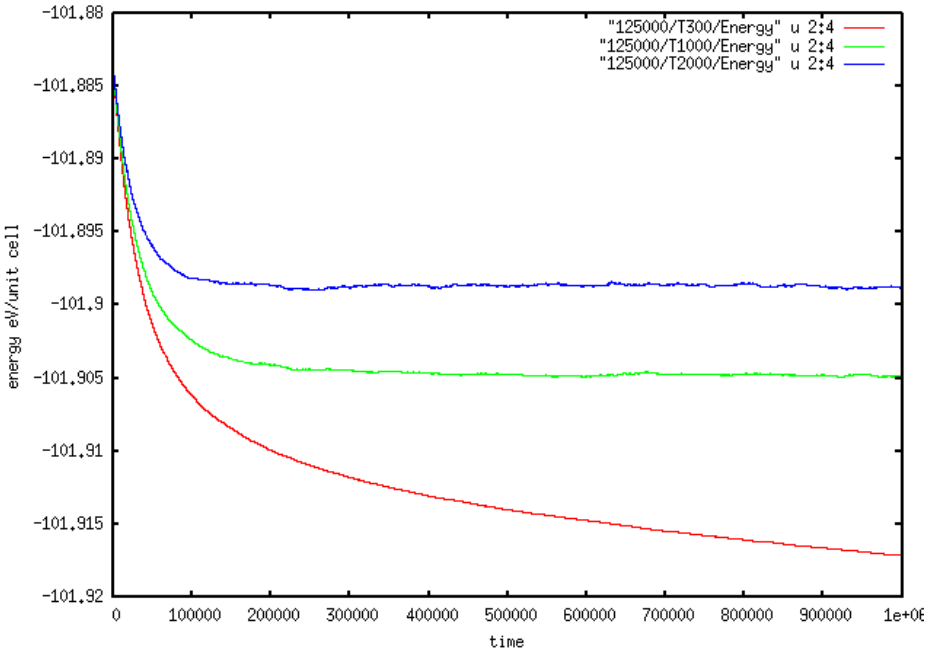

Figure 8 The energies under 300K (red), 1000K (green), and 2000K (blue)

Figure 9 is the energy of the systems with different percentage of C (6.67%, 17.01%, and 26.67%) when the temperature is 1000K. First, the energy of the system with more carbon atoms is lower. Second, the energy does not has a linear relationship with the percentage of carbon atoms. Actually, the energy of the system with 17.01% carbon atoms is lower than the weighted mean value of the energies of the systems with 6.67% and 26.67% carbon atoms. The detail of this phenomena is shown in figure 10. In figure 10, the energy is rescaled that the new "energy" is almost the same in the system with least and most C. It is easy to see that the system with intermediate percentage of carbon atoms does have lower energy than the intermediate energy. Figure 11 and 12 show the same phenomena under 300K and 2000K, respectively.

Figure 13 shows the distribution of carbon in boron carbide $B_{1-x}C_x$. Clearly there are distinct changes in carbon distribution at $B_{13}C_2$ and B_4C where physical properties have gone through distinct changes.

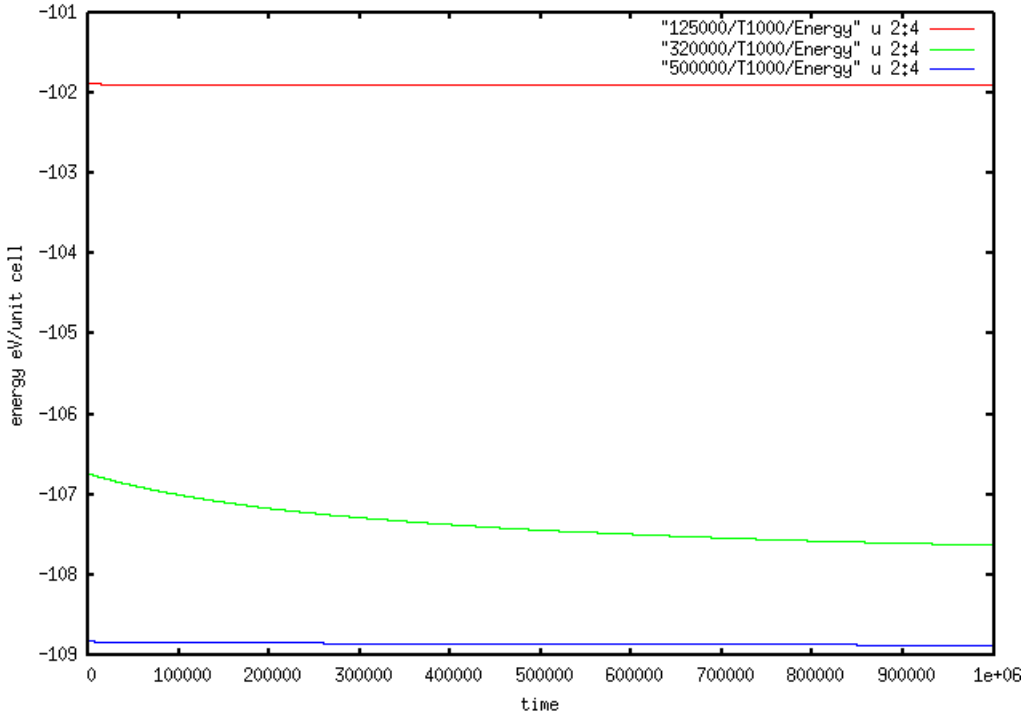

Figure 9 The energies of system with 6.67% (red), 16.67% (green), and 26.67% (blue) carbon atoms

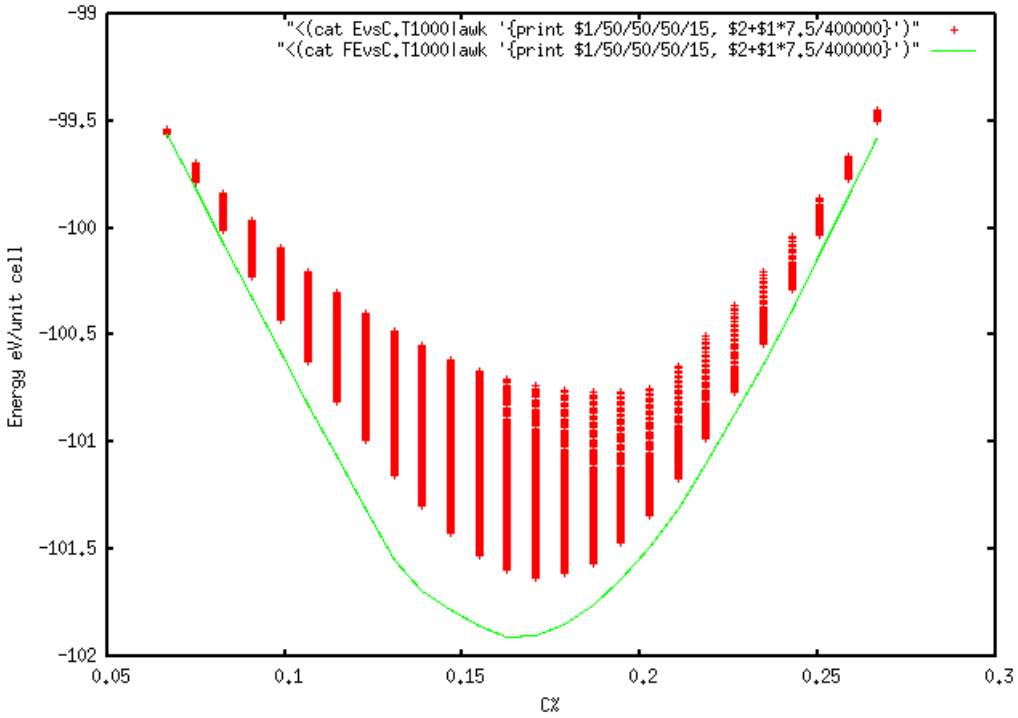

Figure 10 the rescaled free energies (green line) and the convex plot (red crosses). The temperature is 1000K

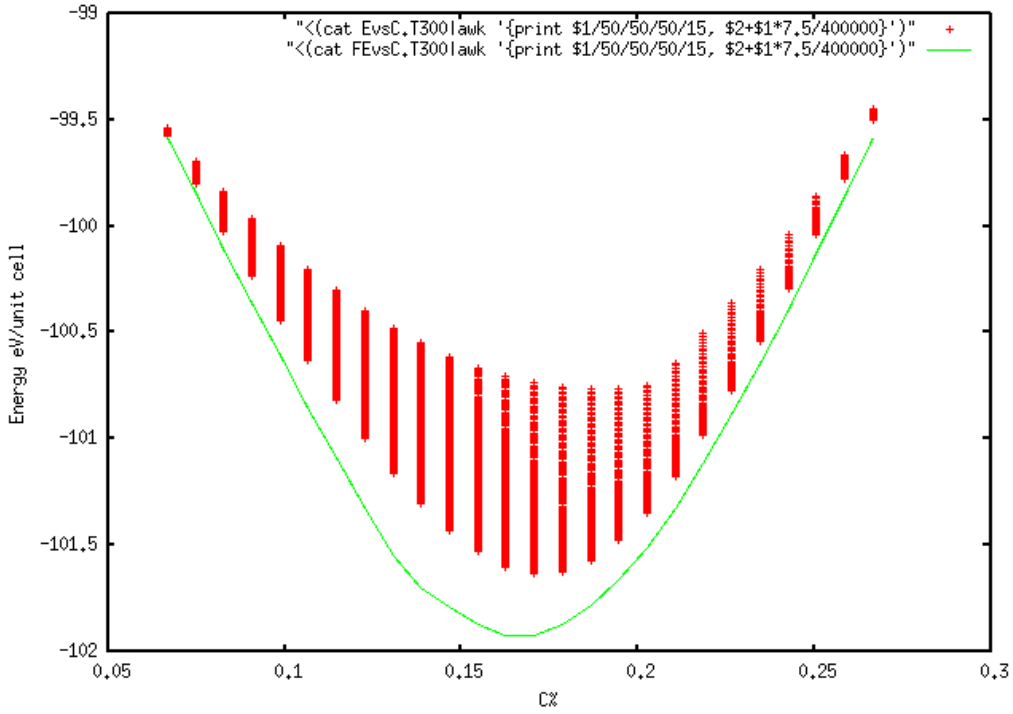

Figure 11 the rescaled free energies (green line) and the convex plot (red crosses). The temperature is 300K

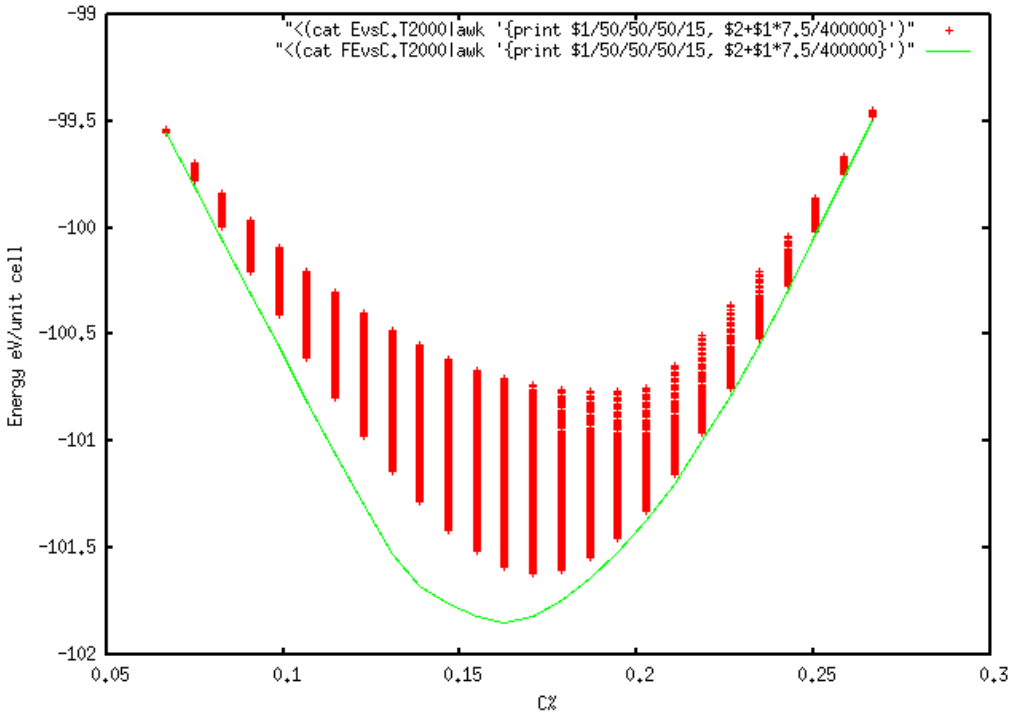

Figure 12 the rescaled free energies (green line) and the convex plot (red crosses). The temperature is 2000K

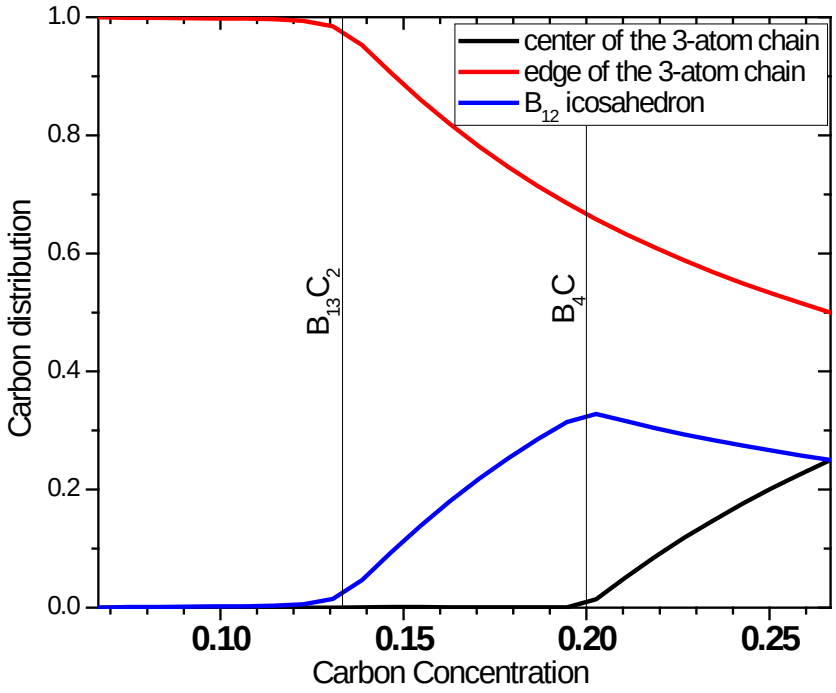

Figure 13. Carbon distribution in Boron carbide $B_{1-x}C_x$. Red line indicates carbon percentage at two edge sites of the 3-atom chain. Blue line shows the carbon percentage in the icosahedrons. Black line depicts carbon percentage at the center of the 3-atom chain.

Z-phase

Figure 14 illustrates the tetragonal unitcell of Cr(Nb,V)N which has five sublattice sites per primitive cell. Among the five sites, two are randomly occupied by Nb or V atoms. Therefore, there are only four possible unitcells and they are all included the unitcell list for UEM calculations. 485 random small supercells are used to estimate the ECIs. Figure 15 shows the estimated ECI vs. the order of the ECI parameter and cross-validation of the chosen cluster expansion cutoff. Clearly, higher order terms (>2) are very small and a maximum order cutoff at two c impact the results.

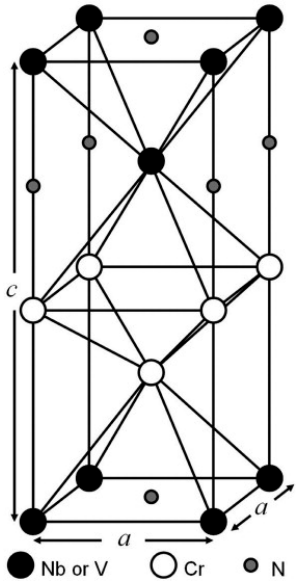

Figure 14. Ball-stick model of Z-phase.

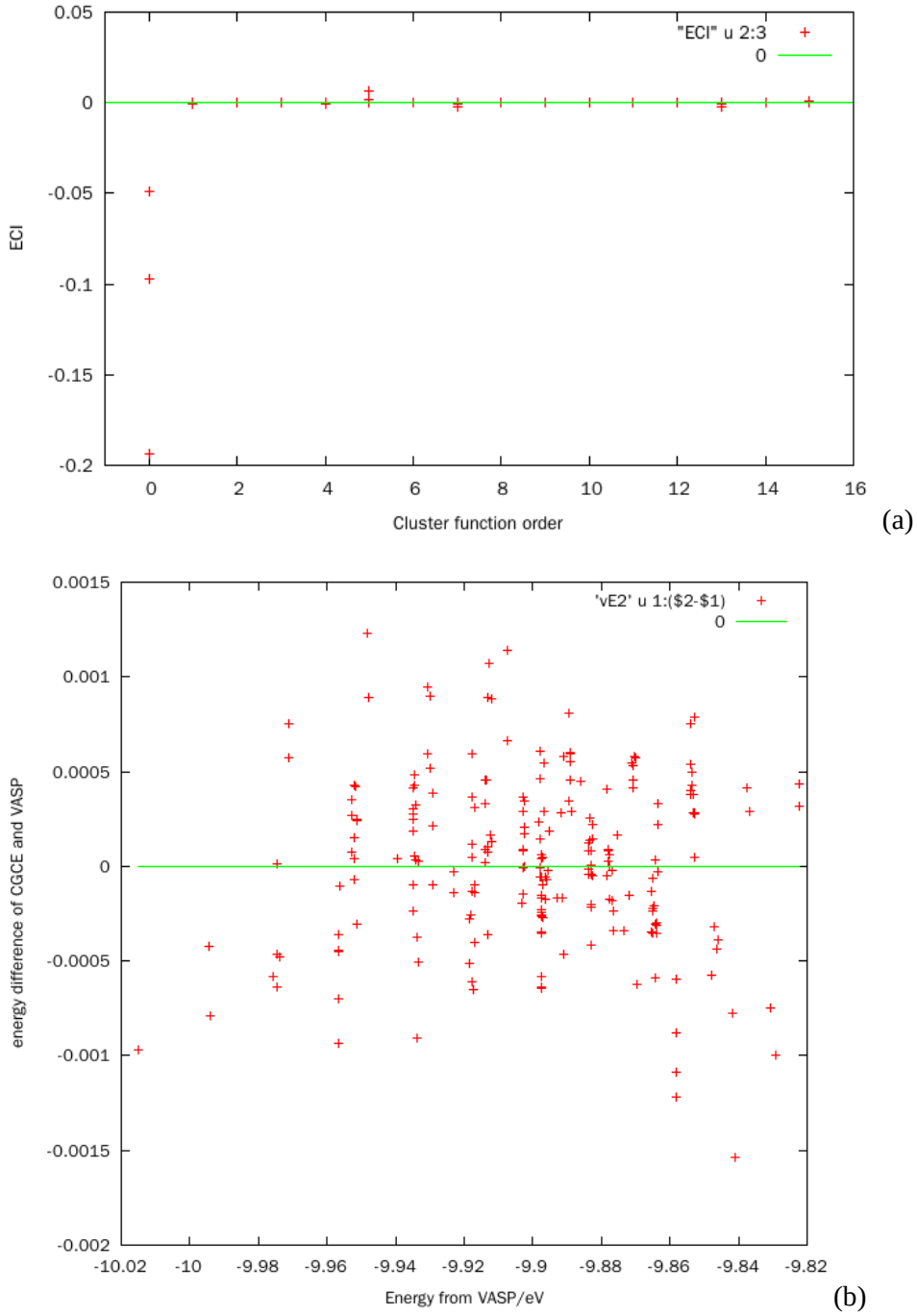

Figure 15. (a) Effective cluster interaction (ECI) versus cluster function order parameter s. (b) Cross-Validation: (energy difference between energies obtained from direct VASP calculations and cluster expansion). ECIs are obtained from different supercell set.

Temperature and Pressure Dependent Elastic Constants Calculations

Silicon Carbide

Silicon carbide (SiC) has wide range of high temperature applications owing to its unique properties such as high hardness, high sublimation temperature, and excellent chemical inertness at high temperatures. It has dozens of polymorphs that consist of different ordered stacking sequences of SiC atomic double layers. Whether the origin of these polymorphs is of thermodynamic nature or non-equilibrium processing has been discussed previously. Because of its vast polymorphs and relative ease of defect formations and impurity inclusions, its high temperature properties measured experimentally are often found to vary significantly in the literature. Thus it is highly desirable to develop reliable and robust methodologies to provide accurate data of thermodynamic and elastic properties for the pure polymorphs from the first-principles calculations as a benchmark reference for its various applications. Extensive researches using first-principles methods have been reported in the literature for its electronic structure, optical properties, and mechanical properties, *etc*. However, calculations of its high temperature elastic properties using first-principles methods have not been reported. In principle, temperature and pressure dependent elastic constants can be calculated from either lattice dynamics or molecules dynamics.

Figure 18 shows the calculated phonon dispersions for both 3C- and 2H-SiC. The calculated zone center modes are listed in Table I. LO/TO splitting due to long range dipole-dipole interaction is included the calculation. The TO and LO frequencies of 3C are in excellent agreement with experimental data.[22] Various thermodynamic properties are calculated using the G(p,T) package. We selectively plot the second order derivatives of Gibbs free energy, specific heat and linear thermal expansion coefficients in Figure 19. At temperature below 700 K,

the calculated specific heat C_p for both 3C and 2H are found to be in good agreement with the experiment.[23] When the temperature reaches 1500 K, the calculated C_p becomes about 6% lower.[24] On the other hand, the calculated thermal expansion coefficients for both phases are slightly larger at higher temperatures if compared to experiments.[25-27] The discrepancies at higher temperature are usually attributed to the anharmonic affect largely due to phonon-phonon interactions that are not included in present calculation. However, other sample preparation related factors such as defect and impurity may also contribute to this discrepancy. It is known that vacancy defects often raises specific heat and thermal expansion coefficient at higher temperature.[28] Recently, Stockmeier *et al* showed that Al and N doping in hexagonal single crystals silicon carbide led to decrease of thermal expansion at higher temperature.[27] At temperature below 100K, our calculation showed a small negative thermal expansion for 3C-SiC contrary to earlier calculations by Tawler *et al*.[29]

To examine the relative thermodynamic stability, we computed their Gibbs free energies for temperature from 0 to 2500 K and pressure from 0 to 20 GPa. At P=0.1 MPa and T=298.15 K, the calculated Gibbs free energy difference between 3C and 2H ($\Delta G=G_{2H}-G_{3C}$) is 0.6 kJ/mol, well within the error range of the experimental value of 1.7±8.9 kJ/mol quoted in the NIST database.[23] Figure 20 shows the contour plot of the Gibbs free energy difference of 3C and 2H. The result indicates that 3C is more stable for the whole temperature and pressure ranges plotted as the Gibbs free energy difference remains positive, which agrees with early calculations reported by Nishitani *et al.*[30] Note that the difference is, however, very small (<1.2 kJ/mol) and it is comparable to the commonly accepted uncertainty for density functional theory based calculations. Nevertheless, the trend indicates increasing temperature will not make 2H more stable than 3C. In fact, using the full-potential linear muffin-tin orbital method, Limpijumnong

and Lambrecht[31] found that 2H has higher energy than 3C by 2.3±0.3 kJ/mol for the four most complete basis sets they considered at zero temperature. On the other hand, earlier theoretical studies[31-33] predict that 4H and 6H are slightly more stable than 3C by <1.9 kJ/mol at zero temperature.

Figure 21 shows the contour plots of the temperature and pressure dependent isotropic polycrystalline shear modulus of 3C and 2H. The shear modulus is calculated using the Voigt-Reuss-Hill (VRH) approximation.[34] Apparently, the two phases of SiC have almost the same shear modulus over the calculated temperature and pressure ranges. Their shear moduli are also slightly higher at the low-temperature high-pressure region than the high-temperature ambient-pressure region. Under ambient pressure, the calculated shear modules are 181 GPa and 166 GPa for 2H at room temperature and 1773 K, respectively, which are in excellent agreements with Munro's measurements of 179±5 GPa and 165±5 GPa for 6H-SiC at the same temperatures.[35] Figure 22 plots the temperature dependent elastic constants at ambient pressure. For 3C, the calculated temperature slopes at elevated temperatures for C_{11}, C_{12}, and C_{44} are -0.024, -0.006, and -0.011 GPa/K, respectively. The temperature slope of C_{11} is in excellent agreement with experimental values of -0.025 GPa/K, while those of the shear moduli C_{12} and C_{44} differ significantly from the measured values, -0.011 and -0.007 GPa/K.[36] For 2H, the calculated elastic constants show better agreement with the experimental value[37] than 3C. The temperature slopes at higher temperature for C_{11}, C_{33}, C_{12}, C_{13}, and C_{44} are -0.014, -0.030, -0.012, 0.001, and -0.006 GPa/K, respectively. To determine the contribution to the elastic constants from thermal excitation, we plotted the elastic constants due to vibrational free energy at zero pressure. The contributions to the elastic constants from vibrational free energy are shown to be significant at elevated temperature particularly for C_{11} and C_{33} which counts about 40% of the

overall temperature slope. At zero temperature, where the vibrational free energy corresponding to the zero point energy, the contribution to elastic modules is generally less than 4 GPa.

In summary, we demonstrated that temperature and pressure dependent elastic constants of solids can be reliably predicted from first-principles method via computing the total Helmholtz free energy. The case with two polymorphs (3C and 2H) of SiC showed the importance to include the vibrational free energy in the elastic constants calculation in order to accurately predict the temperature coefficients particularly at elevated temperature. We believe that the ability to calculate temperature and pressure dependent elastic constants reliably from first-principles method will accelerate new alloy design and development of next-generation high-temperature materials with improved thermal and mechanical stability towards greener energy.

Table I. Zone-centered vibrational modes.

Branch	$\lambda(cm^{-1})$	Branch	(cm^{-1})
2H-SiC		3C-SiC	
E2	256.3	TO	793.5(796.2[a])
B1	589.2	LO	964.2(972.2[a])
E2	740.0		
A1	749.2		
E1(TO/LO)	777.4/941.6		
B1	807.2		

a) Experimental data from Ref.[22]

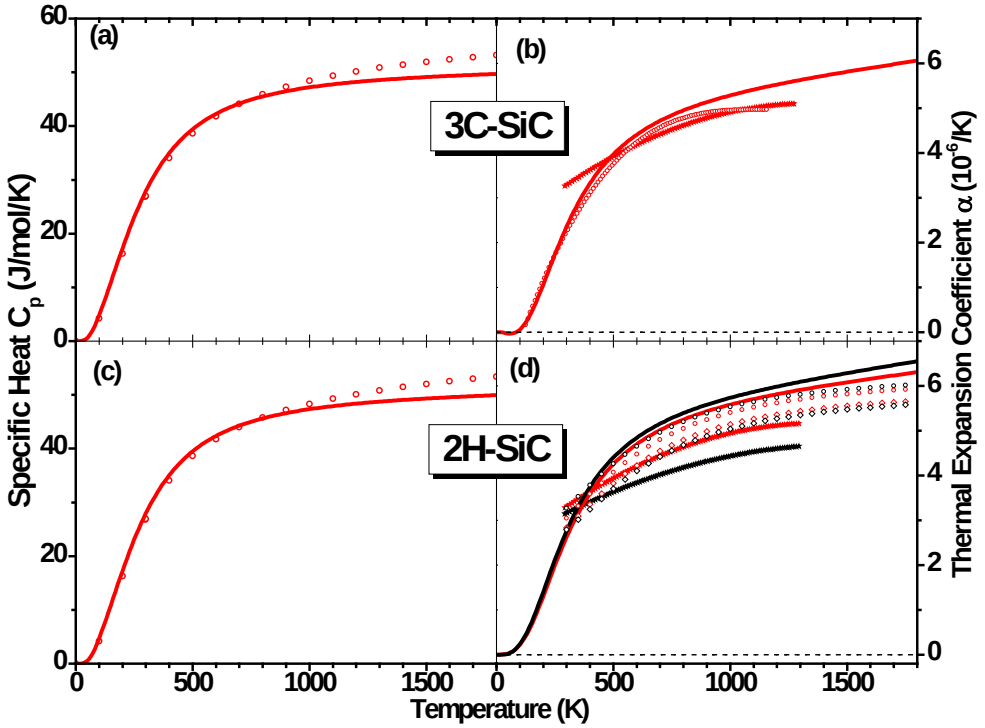

b)

Figure 18. Thermodynamic properties at P=0 up to 1800 K. Solid lines represent the calculated results. (a) Specific heat C_p of 3C. Empty circles are plotted using the experimental data (Ref.[23]) (b) Thermal expansion coefficient of 3C. Empty circles and solid starts are experimental values from Ref.[24] **.** and Ref.[25] **.** respectively. (c) Specific heat C_p of 2H. Empty circles are the experimental data from Ref.[23] (d) Thermal expansion coefficient of 2H. The red symbols are α_{11} and the black symbols are α_{33}. The circles and diamonds are recent data from Ref.[27] **.** for undoped single crystals of 6H-SiC and 4H-SiC, respectively. The solid stars are from Ref.[26]

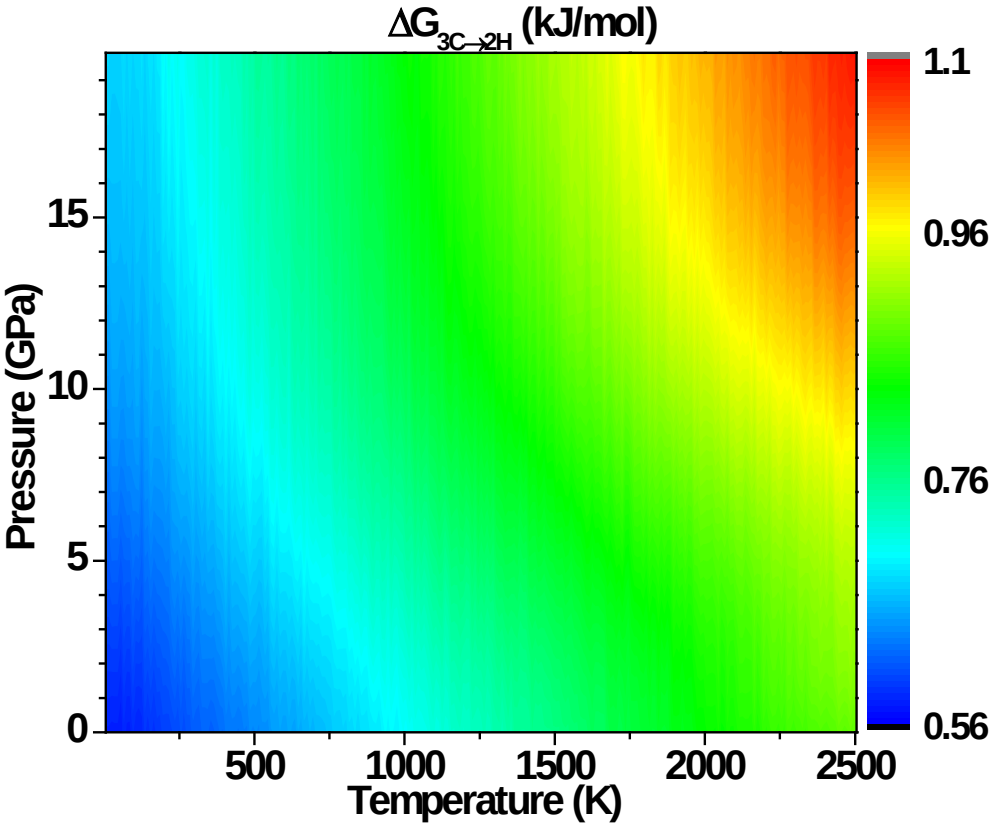

Figure 19. Contour plot of the Gibbs free energy difference from 3C-SiC to 2H-SiC.

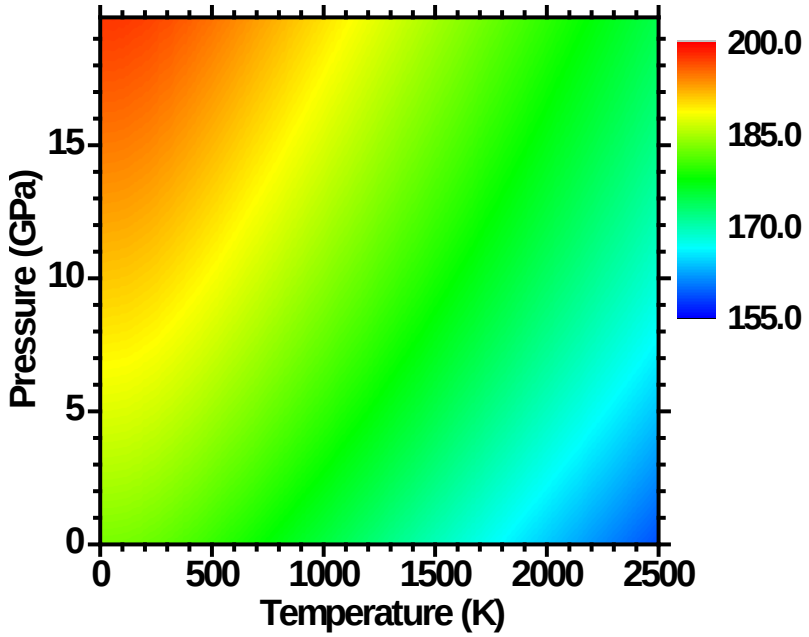

(a)

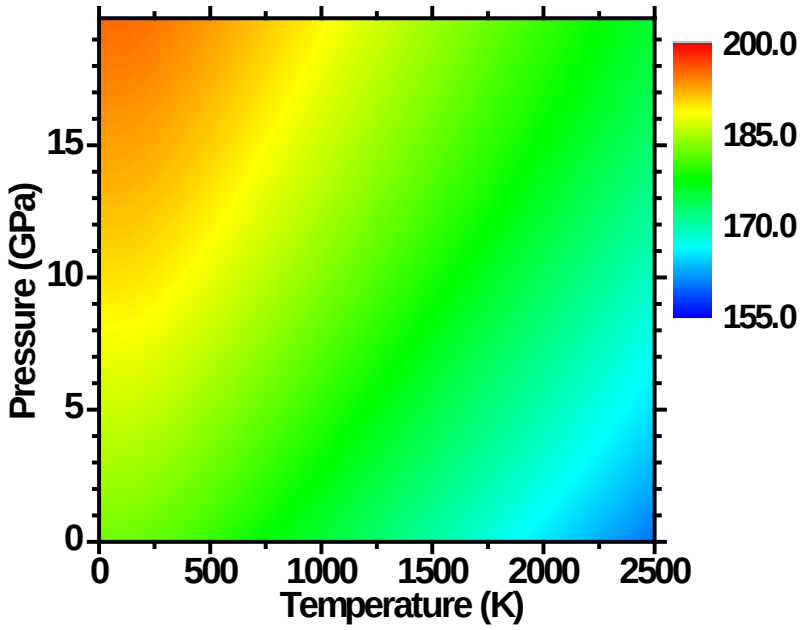

(b)

Figure 3. Contour plots of the temperature pressure dependent shear modulus: (a) 3C-SiC. (b) 2H-SiC.

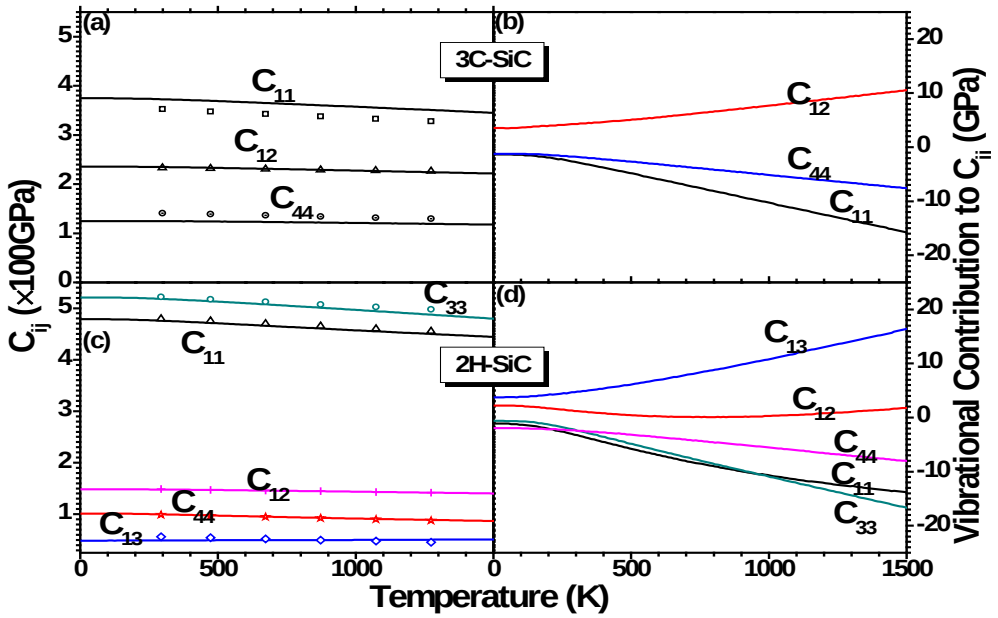

Figure 21. Temperature-dependent elastic constants at ambient pressure. Solid lines are the calculated properties and the symbols are from experimental measurements. (a) and (b) plot the elastic constants and thermal excitation contribution to elastic constants of 3C-SiC. The experimental data are from Ref. [36].. (c) and (d) show the elastic constants and thermal excitation contribution to elastic constants of 2H-SiC. The experimental data are from Ref.[37]

Tungsten

The temperature and pressure dependent elastic constant module implemented in G(p,T) allows calculation of equation of state. To examine the validity of the method, we calculated the equation of state of Tungsten which has extensive experimental data available over a wide range of temperature and pressure. Figure 22 shows the computed the equation of state surface and the dotted points are obtained from shock wave high pressure studies. We observed an excellent agreement between the computed and experimentally measured.

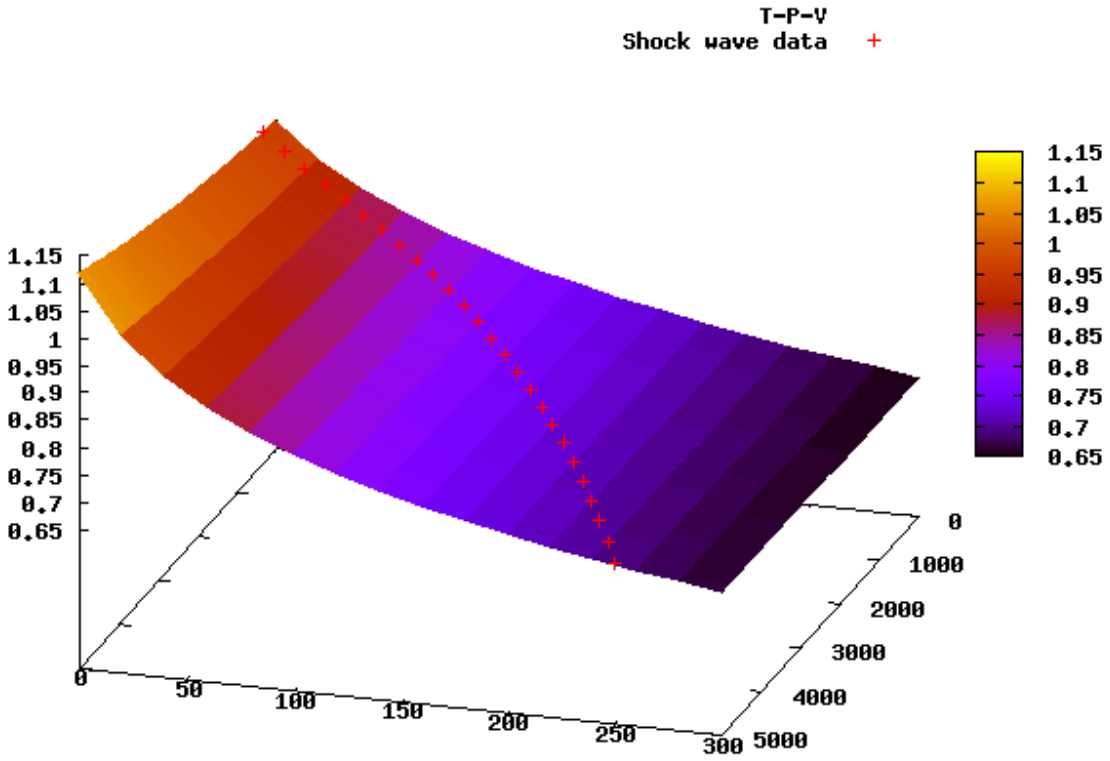

Figure 22. Equation of state P-V-T of Tungsten calculated using the G(p,T) package.

Uni-axial tensile simulation

To examine the uni-axial tensile scheme implemented in G(p,T), we selected simple FCC metal Al as our material. Figure 23 illustrate the energy and stress evolution over the non-uniform pathways.

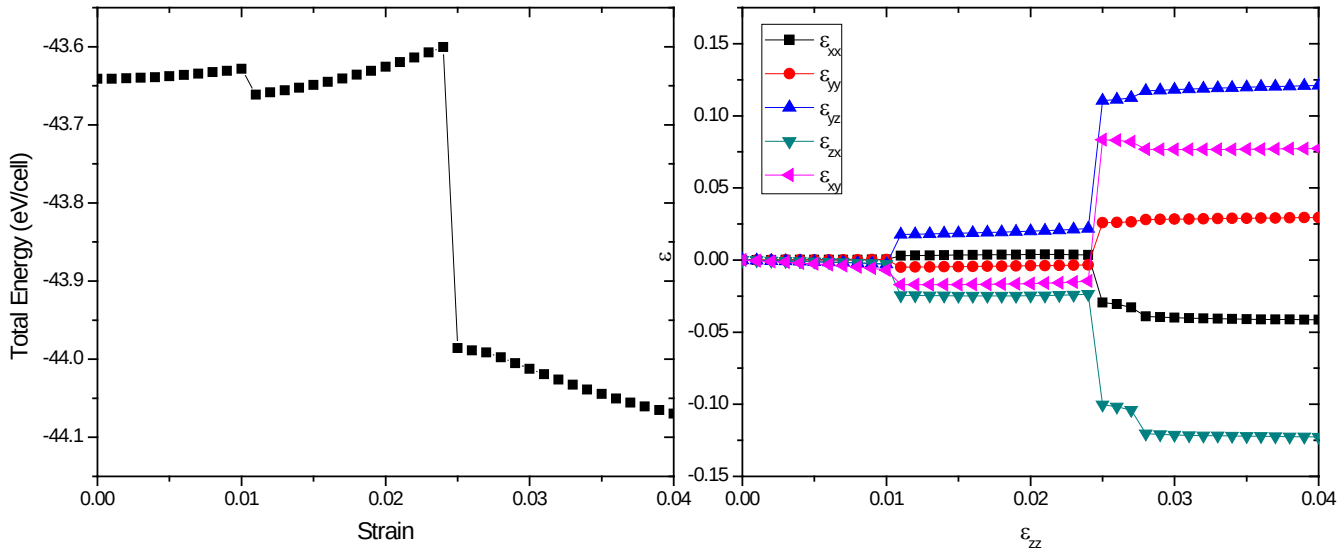

Figure 23. Tensile Simulation on FCC Aluminum. [001] is the tensile direction. Supercell: [1/2a 0 1/2a; 0 1/2a 1/2a; -4a -4a 4a]. Slipping direction preferably [1 0 1] and slipping plane {-1 -1 1}

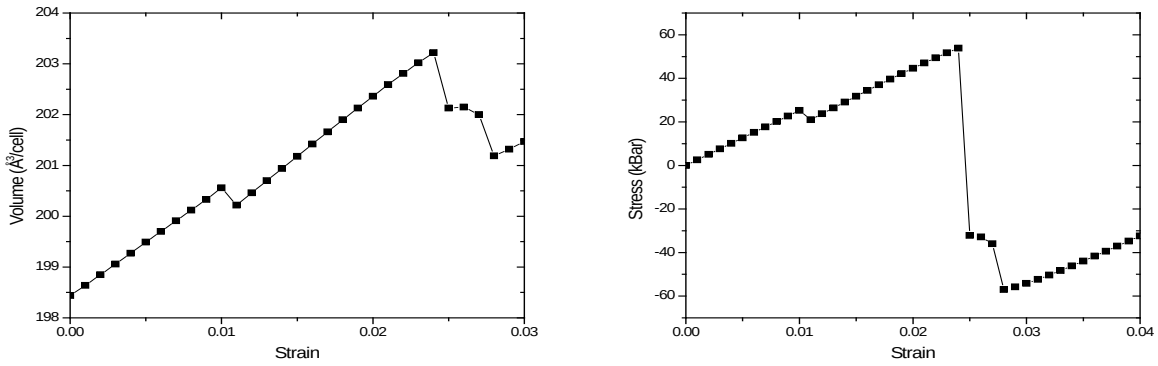

Figure 24. Evolution of volume/stress under uni-axial tensile strain.

FF

Figure 25. Evolution of Al supercell under tensile stress. The relaxation under constant stress using algorithm described in previous section.

The Gensurf program

We have developed a set of useful script tools to generate slab/interface modules. The *gensurf* script can be used generate slab model for a given VASP POSCAR file. By specifying plane miller index, slab position, slab thickness, and vacuum thickness, *gensurf* produces another VASP POSCAR file of the model. Different slabs can be combined by matching the surface basis and origins.

Physical properties of Nb-Si based Alloys

There are six stable solid phases in the Nb-Si binary system: (1) the bcc W-type terminal solid solution of Nb; (2) tetragonal Ti_3P Nb_3Si (tP32); (3) tetragonal W_5Si_3-type β-Nb_5Si_3 (tI32); (4) tetragonal Cr_5Si_3-type α-Nb_5Si_3 (tI32); (5) hexagonal $CrSi_2$-type $NbSi_2$ (hP9); (6) diamond cubic terminal solid solution of Si. Additional meta-stable phases are also reported in the literature including Nb_3Si (tI32), Nb_3Si(cP4), Nb_3Si(cP8), and Nb_3Si_2(tP10). We have systematically studied all crystalline phases in the binary system. First, we calculated the formation enthalpy ΔH of all known binary phases according to,

$$\Delta H = E_p - (xE_{Nb} + (1-x)E_{Si}) \quad (15)$$

where E_p, E_{Nb}, and E_{Si} are the total energy of the binary phase, pure ground state Nb and pure ground state Si, respectively. Figure 26 shows the convex plot of the zero temperature formation energy of the binary Nb-Si phases. The calculations correctly identified the stable binary phases marked as black squares.

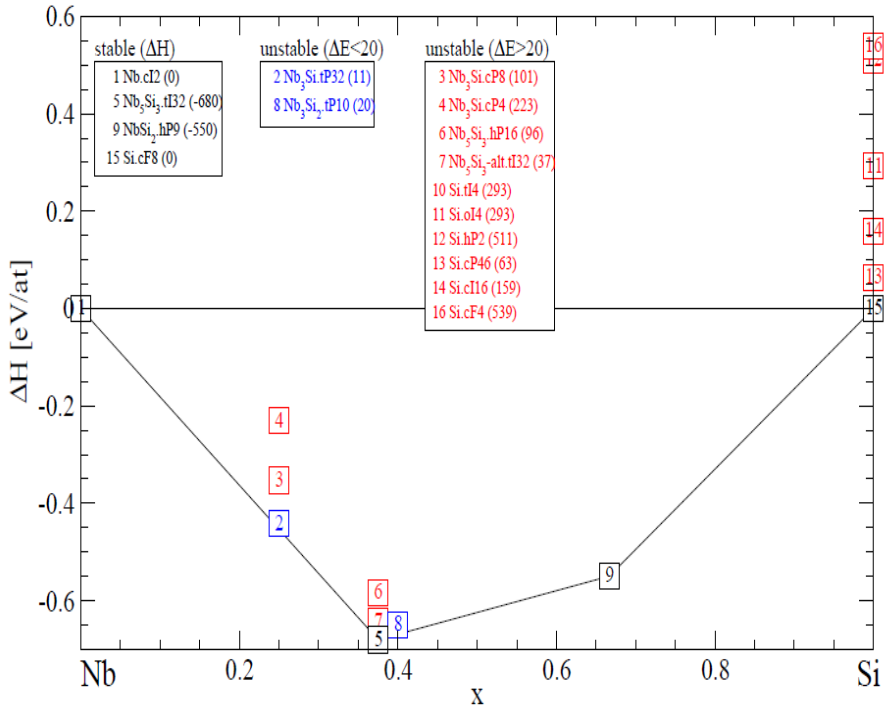

Figure 26. Convex plot of Nb-Si binary phase formation energy.

Mechanical Properties of Nb-Si based alloys

Two G(p,T) modules have been implemented to automated the calculations of pressure dependent elastic constants at zero temperature (*calET*) and both temperature and pressure dependent elastic constants (*calCET*). We calculated the pressure dependent elastic constants of most binary and ternary systems found in the Nb-Si-Cr-Al system. Due to computational resource limit, we only calculated T,P-dependent elastic constants for selected system.

Table II. List of computed elastic constants of Nb-Si binary alloys at zero temperature and zero pressure.

Comp.	Phase	C_{11}	C_{12}	C_{13}	C_{33}	C_{44}	C_{66}	K	G
Nb	cI2								
Nb_3Si	cP4	111	220			72		184	21
	cP8	323	119			68		187	81
	tP32	267	175	133	284	84	95	189	78
Nb_5Si_3	tI32	383	102	121	334	131	121	198	127
	tI32'	381	123	112	329	87	129	198	110
	hP16	327	153	99	359	-1132	87		
Nb_3Si_2	tP10	349	136	127	298	131	118	197	116
$NbSi_2$	hP9	349	76	80	442	126	136	179	138

(Unit: GPa)

Pressure dependent elastic constants at zero temperature

The pressure dependent elastic constants of Nb-Si alloy phases are calculated used the G(p,T) package. Due to the high computational cost of temperature dependent elastic constant, we performed temperature dependent elastic constant for only selected systems and the rest are calculated at zero temperature. The method is described in previous sections (Equation 10). In the following section, we summarized the calculated pressure dependent elastic constant of binary, ternary alloy phases. The electronic structure of the systems have been examined and compared with results published in the literature whenever available. To limit the amount of diagrams in this report, we plotted only the pressure dependent elastic constants at zero temperature.

Binary phases

(1) Nb-Si

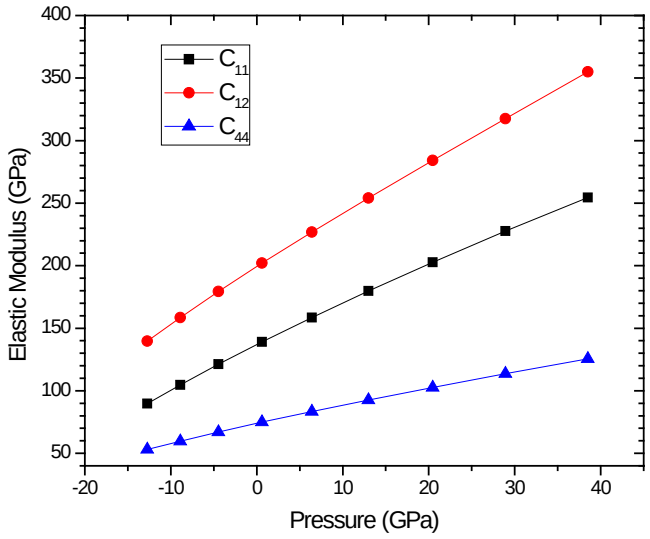

Figure 27. Pressure dependent elastic constants of Nb_3Si(cP4)

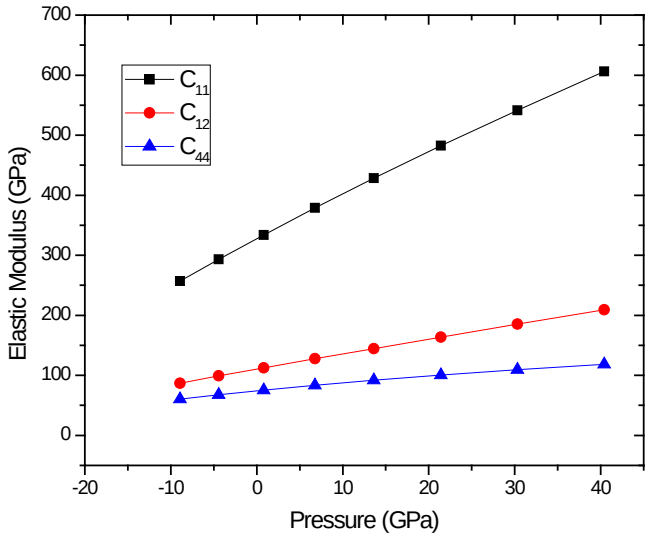

Figure 28. Pressure dependent elastic constants of Nb_3Si(cP8)

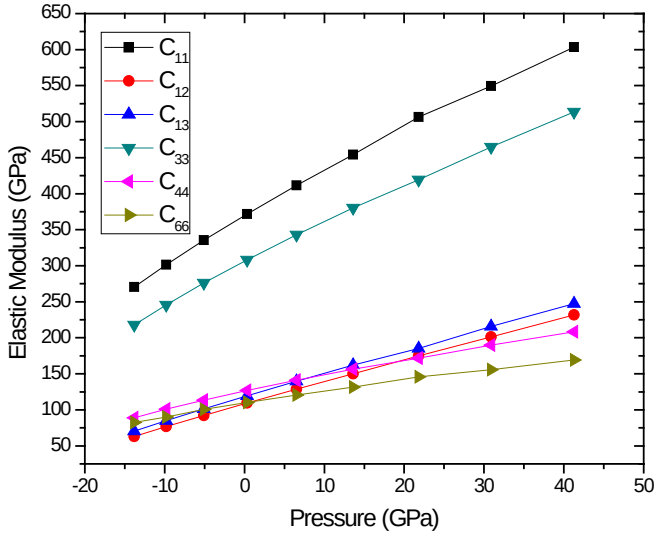

Figure 29. Pressure dependent elastic constants of Nb_3Si_2(hP9)

(2) Cr-Si

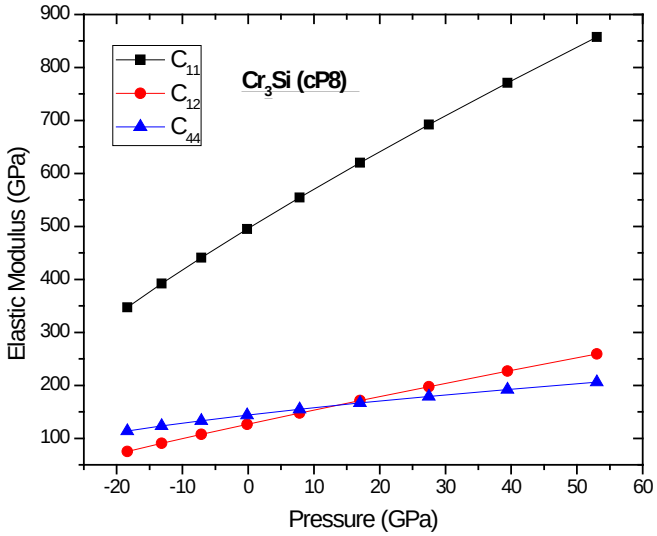

Figure 30. Pressure dependent elastic constant of Cr_3Si(cP8)

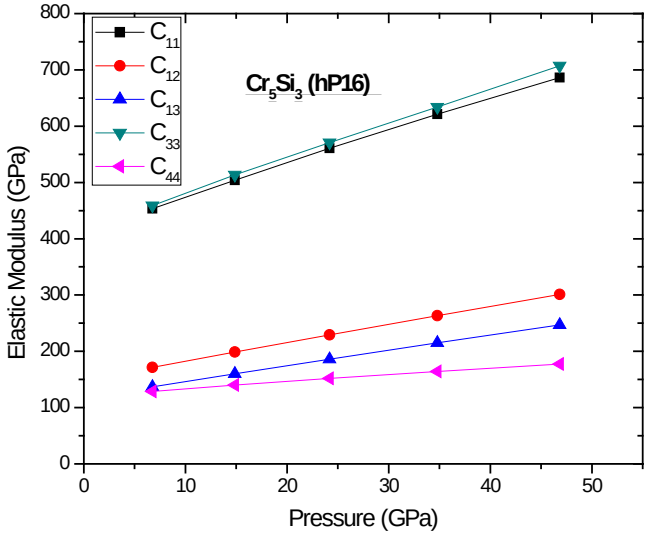

Figure 31. Pressure dependent elastic constants of Cr_5Si_3 (hP16).

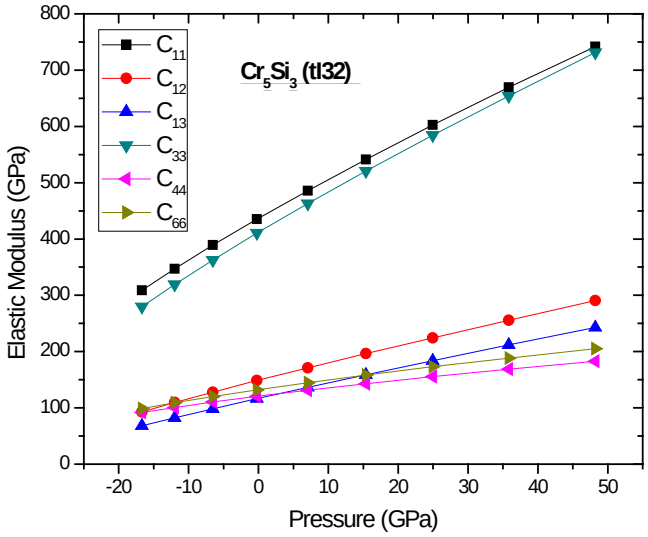

Figure 29. Pressure dependent elastic constants of Cr_5Si_3(tI32).

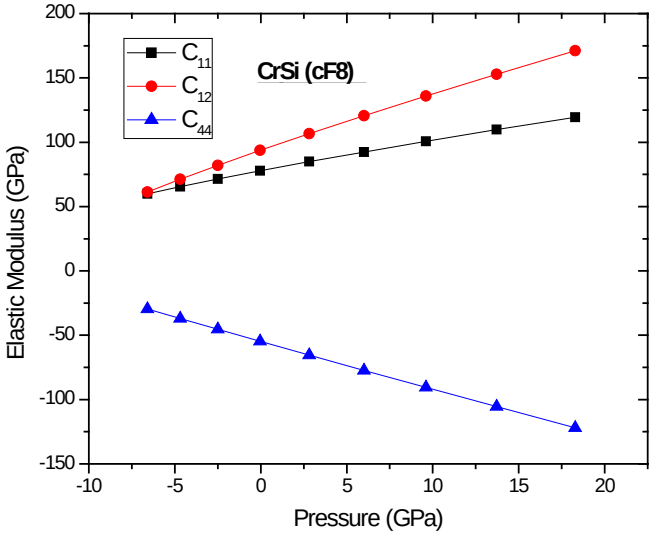

Figure 30. Pressure dependent elastic constants of CrSi(cF8). It is clearly an unstable structure.

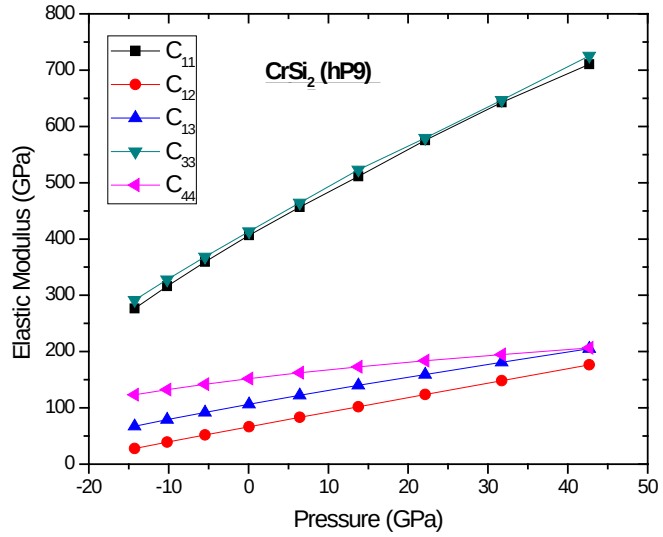

Figure 31. Pressure dependent elastic constants of $CrSi_2$(hP9)

(3) Nb-Cr

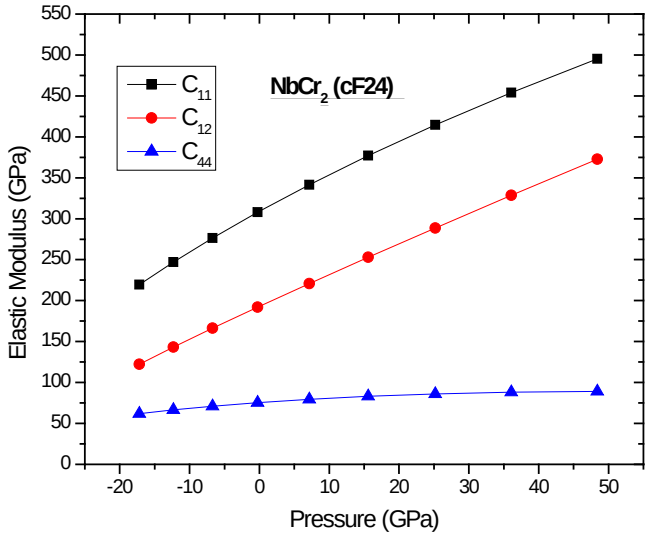

Figure 32. Pressure dependent elastic constants of $NbCr_2$(cF24)

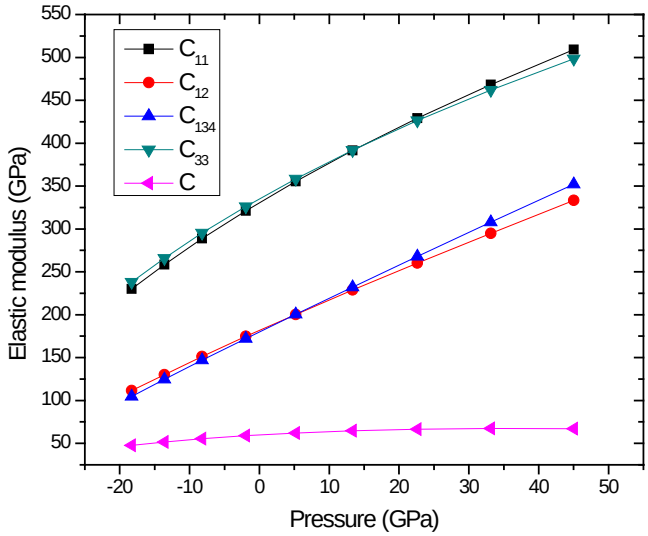

Figure 33. Pressure dependent $NbCr_2$ (hP12)

Ternary phases

(1) Nb-Cr-Si

a. Nb_2CrSi_3 (hP12)

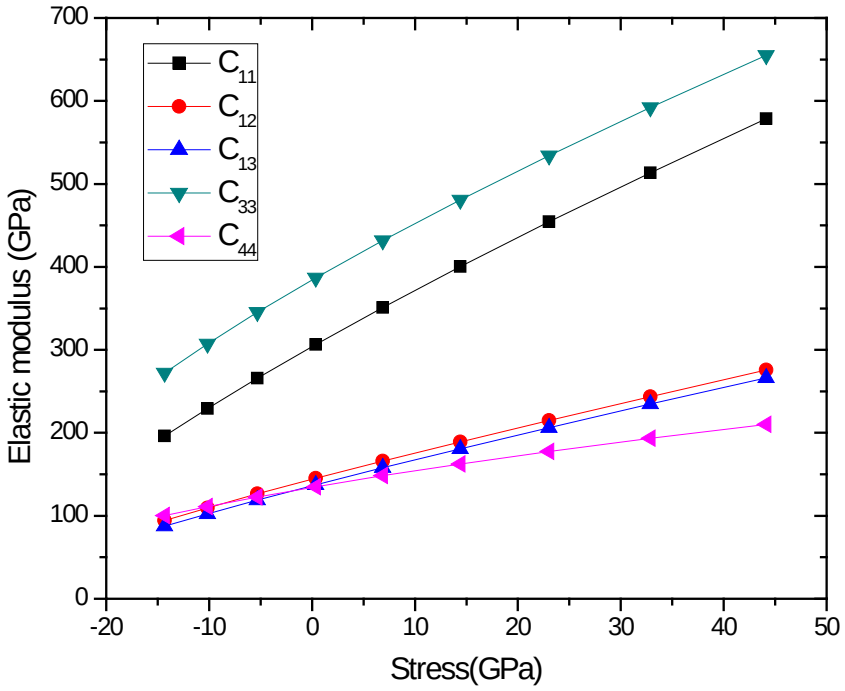

Figure 34. Pressure dependent elastic constants of Nb_2CrSi_3(hP12)

b. Nb_2Cr_3Si (hP12)

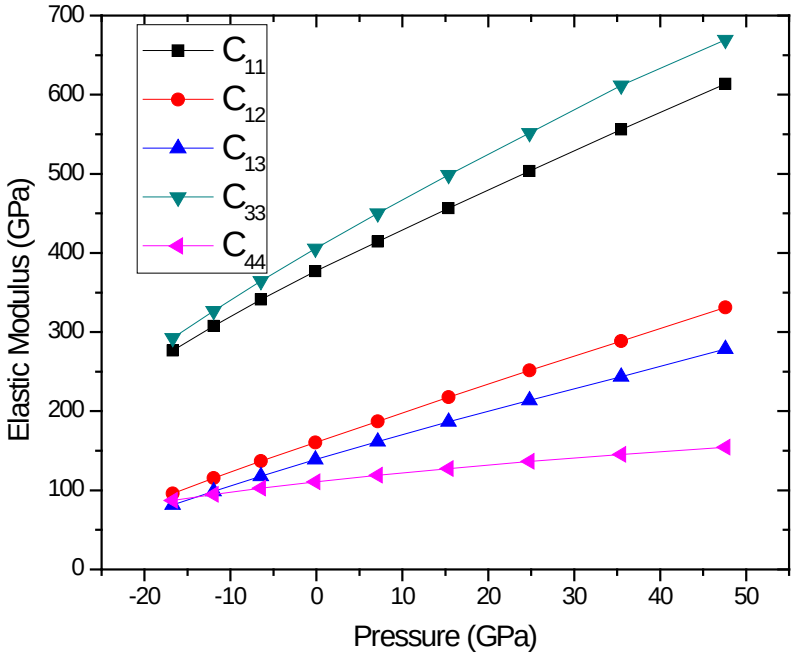

Figure 35. Pressure dependent elastic constants of Nb_2Cr_3Si (hP12)

Phonon dispersion of Nb-Si based alloy

Binary systems:

(1) Nb-Si system

a. Nb_3Si (cP8)

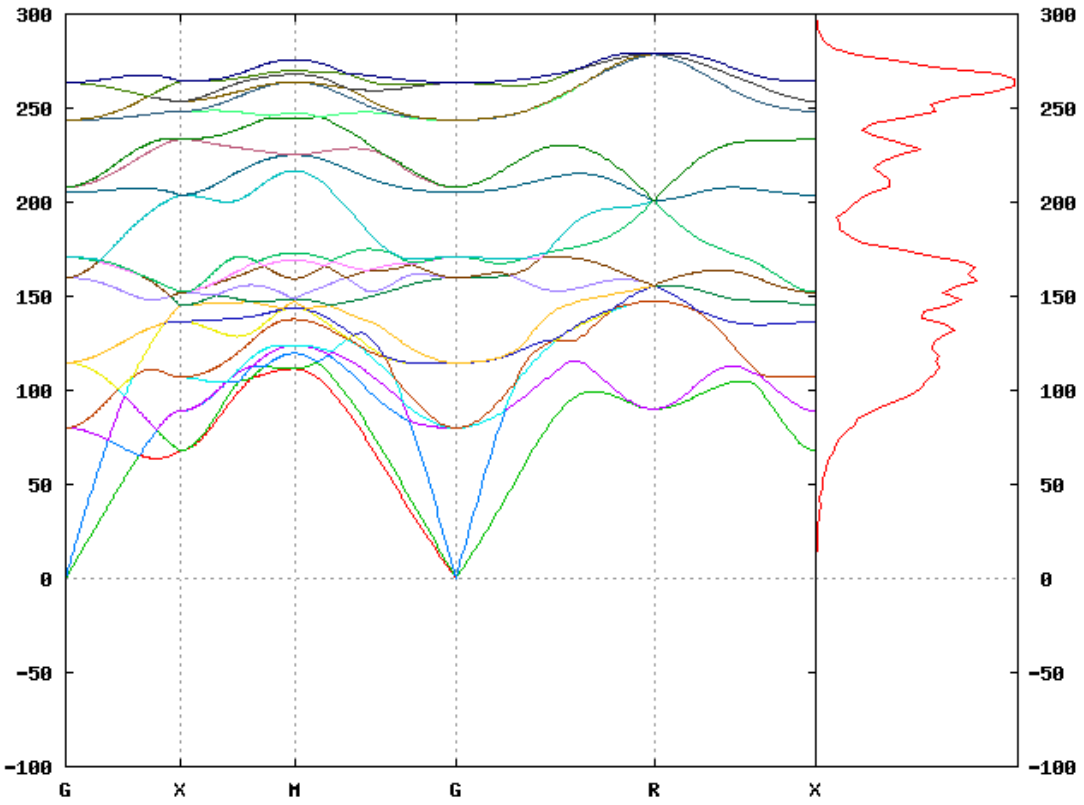

Figure 36. Phonon dispersion of Nb_3Si(cP8).

Linear Thermal Expansion Coefficient of Pure Nb

Figure 37 plot the calculated linear thermal expansion coefficient of pure Nb at zero pressure. The calculated results of 8.02×10^{-6}/K at zero pressure and room temperature is in very good agreement with experim7nts (7.75×10^{-6}/K) [38].

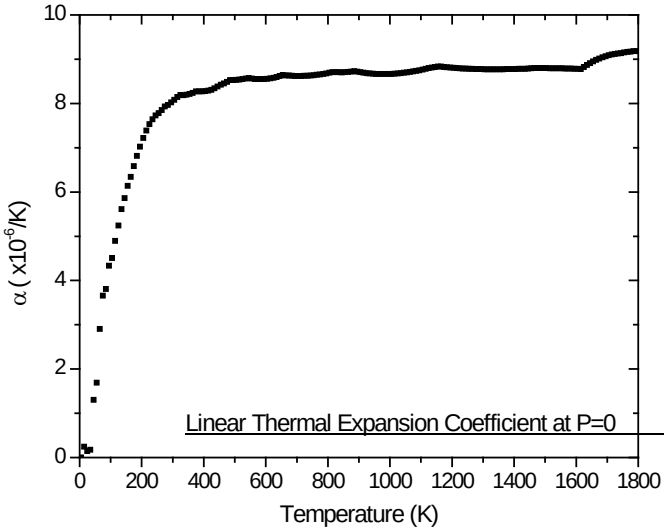

Figure 37.linear thermal expansion coefficient of pure Nb from calculations.

Figure 38 shows the zero pressure temperature dependent elastic constants of pure Nb. To understand the contribution to elastic constant from lattice vibration, we plot the part of elastic constants only from vibrational free energy. It is clearly, the contribution of electronic part of the free energy, decreasing as temperature increases since volume expanded, cancels the contribution of the lattice vibration which are largely increasing with temperature. The C_{12} appears flat throughout a wide temperature range and C_{44} shows significant temperature hardening.

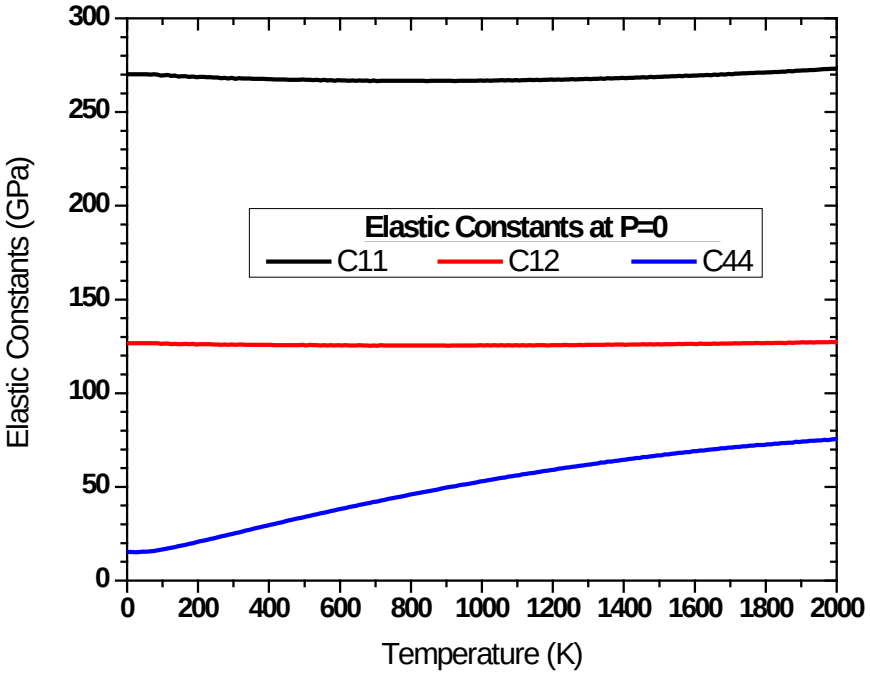

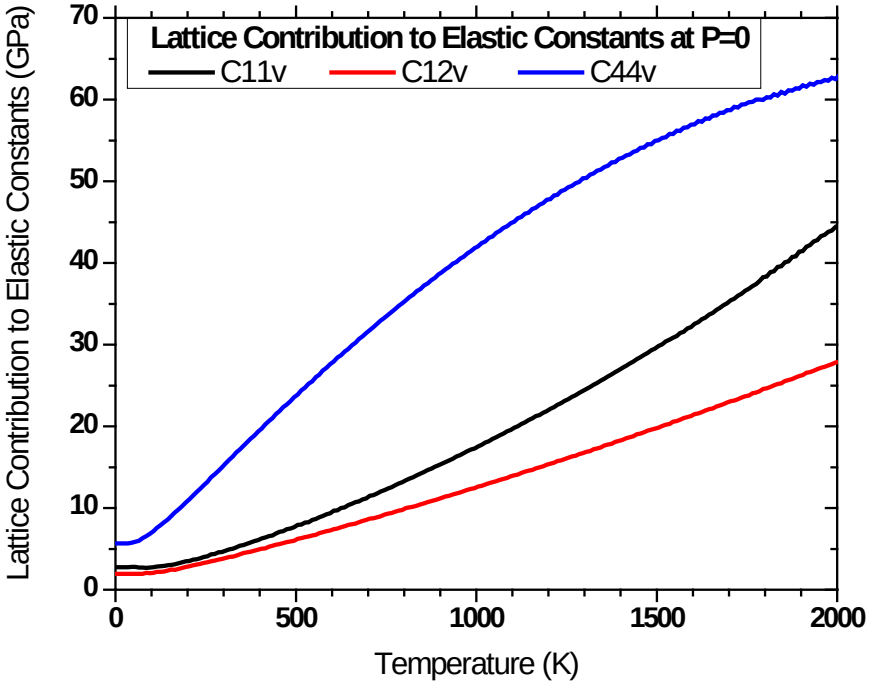

Figure 38. Temperature dependent elastic constant of Nb pure metal.

Contour plots of thermodynamic properties:

The temperature and pressure dependent thermodynamic properties calculations are computationally expensive. Here we report three phases that such calculations had been performed: Si(cF8), Nb(cI2), and Nb_3Si(tI32). While many thermodynamic properties calculated, we plot here only the Gibbs free energy, bulk modulus, and thermal expansion coefficient, which are 0^{th}, 1^{st}, and 2^{nd} order derivatives of free energy, to illustrate the accuracy of the calculations.

(1) Pure Si (cF8)

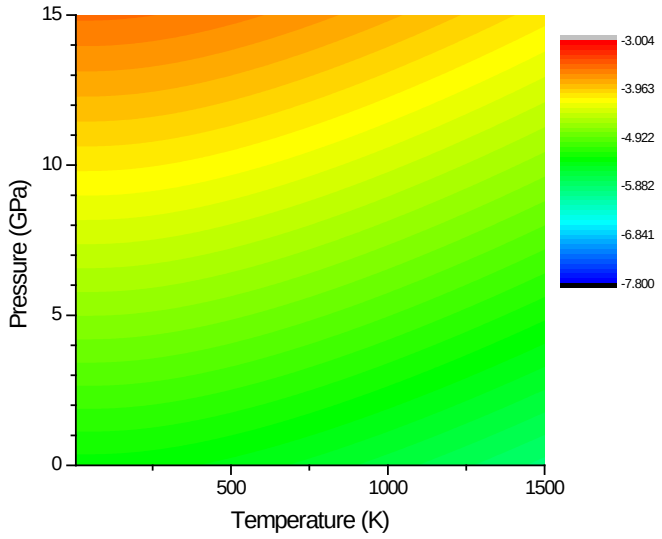

Figure 39. Temperature and Pressure dependent Gibbs free energy of Si (cF8)

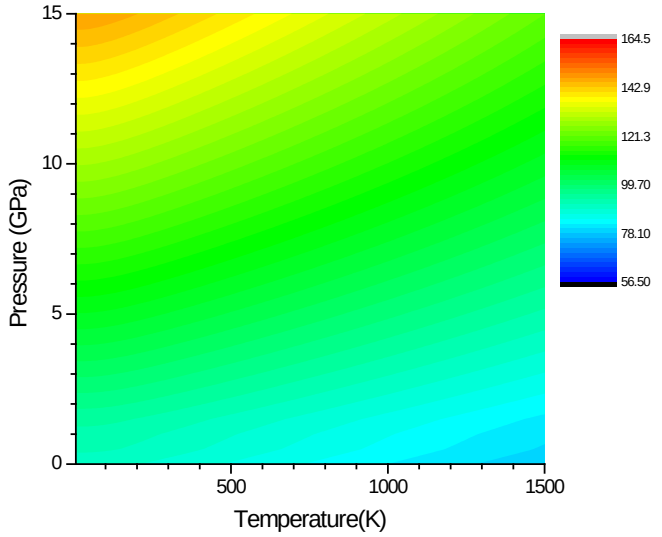

Figure 40. Temperature and Pressure dependent bulk modulus of Si (cF8)

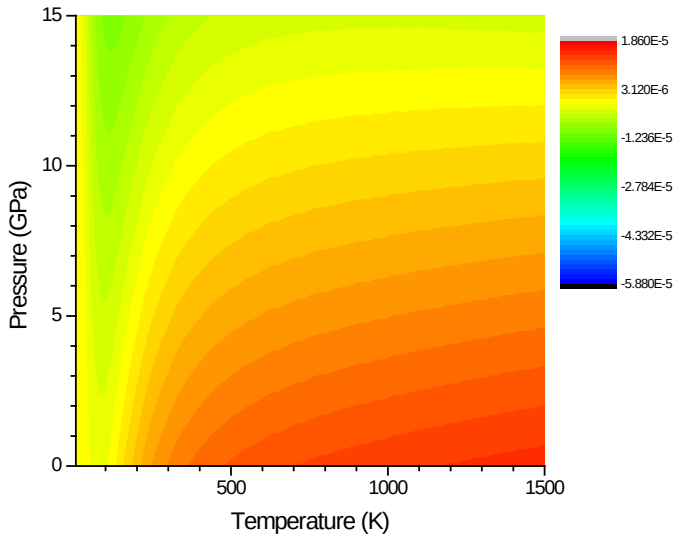

Figure 41. Temperature and Pressure dependent thermal expansion coefficient of Si (cF8)

(2) Nb (cI2)

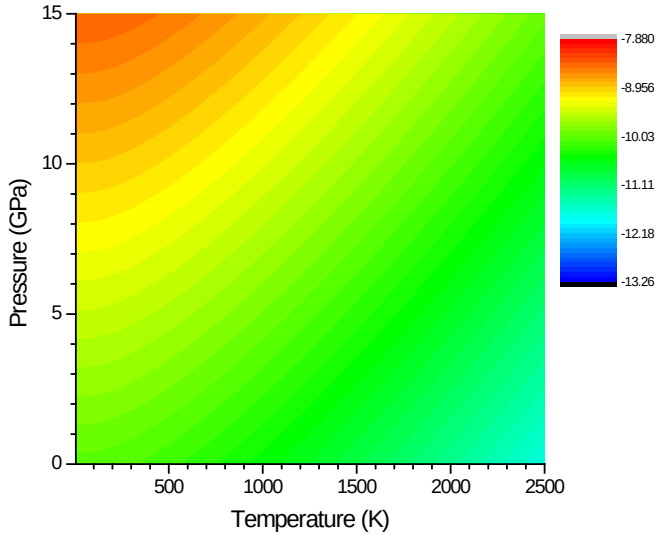

Figure 42. Temperature and Pressure dependent Gibbs free energy of Nb (cI2)

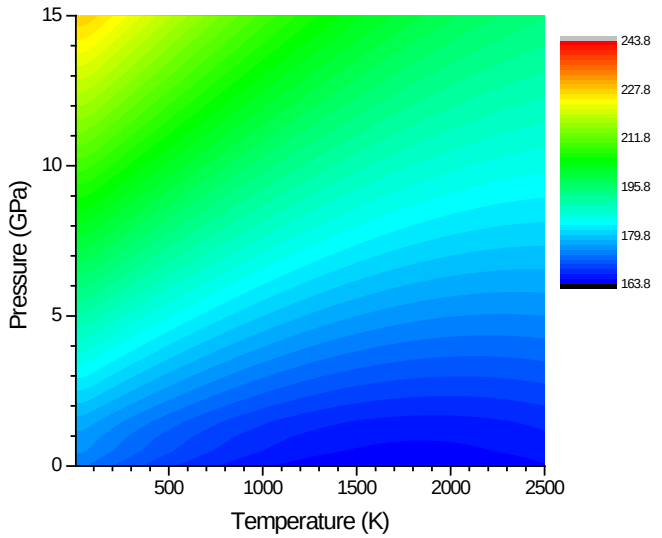

Figure 43. Temperature and Pressure dependent bulk modulus of Nb (cI2)

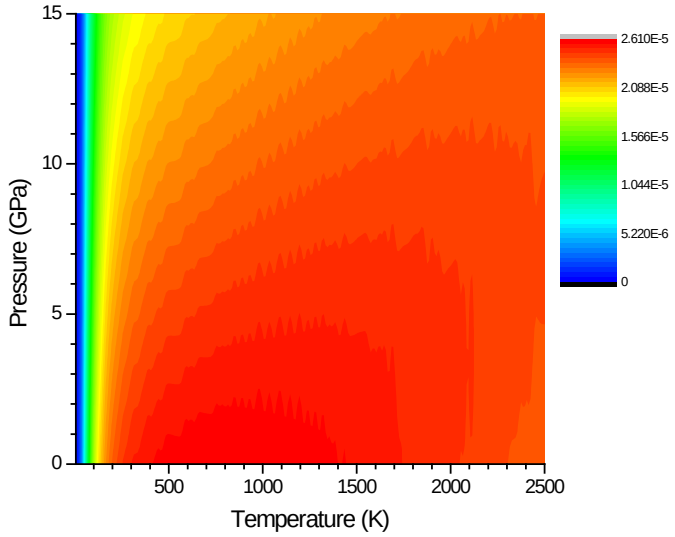

Figure 44. Temperature and Pressure dependent thermal expansion coefficient of Nb (cI2)

(3) Nb_3Si (tI32)

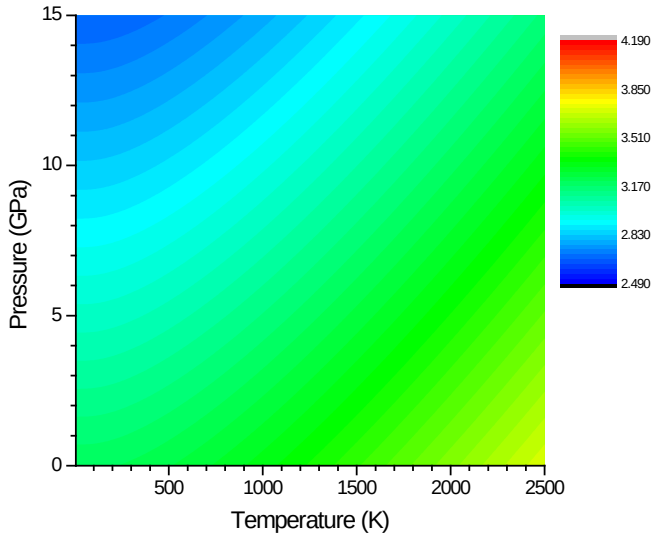

Figure 45. Temperature and Pressure dependent Gibbs free energy of Nb_3Si (tI32).

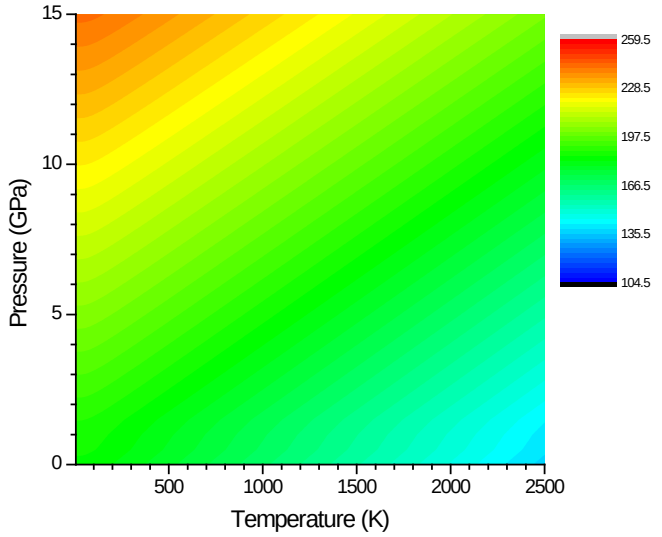

Figure 46. Temperature and Pressure dependent bulk modulus of Nb_3Si (tI32).

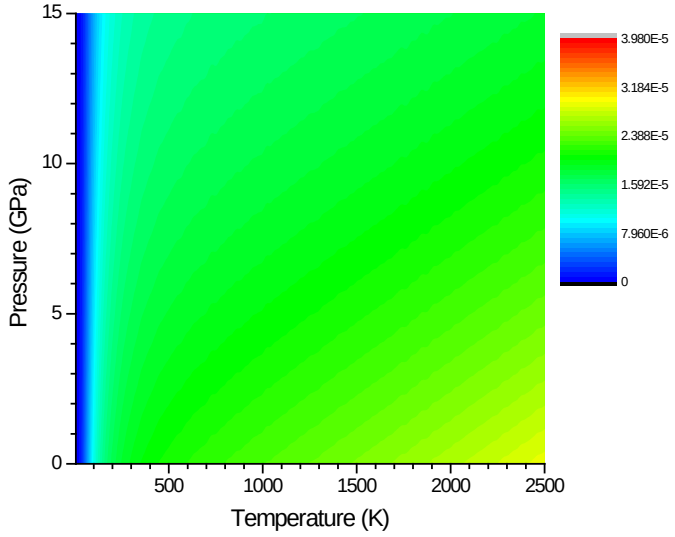

Figure 47. Temperature and Pressure dependent thermal expansion coefficient of Nb_3Si (tI32).

CONCLUSIONS

In conclusion, we have further extended the G(p,T) package to calculate temperature-pressure dependent thermodynamic, mechanical properties of crystals; developed a uniaxial tensile simulation modules which allows non-uniform deformation; developed a coarse-grained cluster expansion method which can be used to study complex or dilute solid solution systems. The accuracy of the temperature-dependent elastic constant module was demonstrated in the SiC calculations in which excellent agreement has been obtained (less than 1% error in elastic modulus). The coarse grained cluster expansion was also tested in the Boron carbide and Z-phase system. However, these calculations are computationally very expensive, requiring typically thousands of supercell calculations, which may be not suitable for large scale material screening. A simpler approximation to cluster expansion method at high temperature, the special quasirandom structure (SQS) may be more appropriate method for calculating large number of solid solution structures. Nevertheless, it provided a method for quality checking of SQS calculations.

We have systematically studies mechanical properties of Nb-Si based alloys. We developed modules to automate such complex calculations. With only a structure input in the format of GULP input or CIF, we can complete the calculation with a few lines of shell script.

We have evaluated pressure dependent elastic properties of binary and ternary systems including Nb-Si, Cr-Si, Nb-Cr, and Nb-Cr-Si. We had compiled a structure databases for most of the phases involved in the Nb-Si-Al-Cr-W system. However, due to limited computational resources, only selected crystal phases were completed. We will continue the calculation beyond the project period.

V. FACILITIES AND RESOURCES

We have built a 36-node cluster using AMD phenom™ 6-core and 8-core CPU, and Intel 4-core hyperthread CPU. Among them, 34 nodes are dedicated to computing, 1 node serves as head node that provides internet interface and cluster management, and 1 node is dedicated to storage service. Each computing node has 8GB memory. All computer nodes use a small 40-60GB solid state disk for boot and temporary scratches. An 8TB storage array is used to provide the shared cluster file system.

REFERENCES,

[1] B. Bewlay, M. Jackson, P. Subramanian, J. Zhao, Metallurgical and Materials Transactions A 34 (2003) 2043-2052.
[2] C. Bouillet, D. Ciosmak, M. Lallemant, C. Laruelle, J.J. Heizmann, Solid State Ionics 101-103 (1997) 819-824.
[3] M.J. Davidson, M. Biberger, A.K. Mukherjee, Scripta Metallurgica et Materialia 27 (1992) 1829-1834.
[4] K. Zelenitsas, P. Tsakiropoulos, Materials Science and Engineering: A 416 (2006) 269-280.
[5] J. Geng, P. Tsakiropoulos, Intermetallics 15 (2007) 382-395.
[6] J. Geng, P. Tsakiropoulos, G. Shao, Materials Science and Engineering: A 441 (2006) 26-38.
[7] Y.X. Tian, J.T. Guo, Y.C. Liang, C.L. Wu, L.Z. Zhou, H.Q. Ye, International Journal of Materials Research 98 (2007) 511-515.
[8] J.T. Guo, Y.X. Tian, G.M. Cheng, L.Z. Zhou, L.L. He, H.Q. Ye, Journal of Alloys and Compounds 470 (2009) 606-609.
[9] W.-Y. Kim, H. Tanaka, A. Kasama, R. Tanaka, S. Hanada, Intermetallics 9 (2001) 521-527.
[10] S. Miura, K. Ohkubo, T. Mohri, Intermetallics 15 (2007) 783-790.
[11] H. Lukas, S.G. Fries, B. Sundman, Computational Thermodynamics: The Calphad Method, Cambridge University Press, New York, 2007.
[12] G. Kresse, J. Furthm 黧 ler, Computational Materials Science 6 (1996) 15-50.
[13] G. Kresse, J. Furthm 黧 ler, Physical Review B 54 (1996) 11169.
[14] G. Kresse, J. Hafner, Physical Review B 47 (1993) 558.
[15] H. Yao, L. Ouyang, W.-Y. Ching, Journal of the American Ceramic Society 90 (2007) 3194-3204.
[16] L. Ouyang, W.-Y. Ching, physica status solidi (b) 242 (2005) R64-R66.
[17] L. Ouyang, W.Y. Ching, Journal of Applied Physics 95 (2004) 7918-7924.
[18] L. Ouyang, S. Aryal, P. Rulis, W.Y. Ching, (2008).
[19] M. Friák, M. Šob, V. Vitek, Physical Review B 68 (2003) 184101.
[20] T. Li, J.W. Morris, D.C. Chrzan, Physical Review B 70 (2004) 054107.
[21] M. Černý, J. Pokluda, Physical Review B 82 (2010) 174106.
[22] D.W. Feldman, J.H. Parker, W.J. Choyke, L. Patrick, Phys. Rev. 173 (1968) 787-&.
[23] M.W. Chase, NIST-JANAF Thermochemical Tables, 1998.
[24] P.s.f.D.C.C. http://www.dow.com.
[25] Z. Li, R.C. Bradt, J. Mat. Sci. 21 (1986) 4366-4368.
[26] Z. Li, R.C. Bradt, J. Am. Cera. Soc. 70 (1987) 445-448.
[27] M. Stockmeier, R. Müller, S.A. Sakwe, P.J. Wellmann, A. Magerl, J. Appl. Phys. 105 (2009).
[28] R.E. Taylor, Thermal Expansion of Solids, Asm Intl, 1998.
[29] D.N. Talwar, J.C. Sherbondy, Appl. Phys. Lett. 67 (1995) 3301-3303.
[30] S.R. Nishitani, R. Takeda, H. Ishii, Y. Yamamoto, T. Kaneko, J. Japan Inst. Metals 73 (2009) 566-570.
[31] S. Limpijumnong, W.R.L. Lambrecht, Phys. Rev. B 57 (1998) 12017-12022.
[32] M.J. Rutter, V. Heine, J. Phys.: Cond. Matt. 9 (1997) 8213.
[33] E. Konstantinova, M.J.V. Bell, V. Anjos, Intermetallics 16 (2008) 1040-1042.
[34] R. Hill, Proc. Phys. Soc. London Sec. A 65 (1952) 349-355.
[35] R.G. Munro, J. Phys. Chem. Ref. Data 26 (1997) 1195-1203.
[36] Z. Li, R.C. Bradt, J. Mat. Sci. 22 (1987) 2557-2559.
[37] Z. Li, R.C. Bradt, Intl. J. Hi. Tech. Ceram. 4 (1988) 1.
[38] M.E. Straumanis, S. Zyszczynski, Journal of Applied Crystallography 3 (1970) 1-6.